SMALL ORGAN4 Is a Ribosome Biogenesis Factor Involved in 5.8S Ribosomal RNA Maturation[1][OPEN]

Rosa Micol-Ponce,[a,2,3] Raquel Sarmiento-Mañús,[a,2] Sara Fontcuberta-Cervera,[a] Adrián Cabezas-Fuster,[a] Anne de Bures,[b,c] Julio Sáez-Vásquez,[b,c] and María Rosa Ponce[a,4,5]

[a]Instituto de Bioingeniería, Universidad Miguel Hernández, Campus de Elche, 03202 Elche, Alicante, Spain
[b]Centre National de la Recherche Scientifique, Laboratoire Génome et Développement des Plantes, Unité Mixte de Recherche 5096, 66860 Perpignan, France
[c]Universite Perpignan Via Domitia, Laboratoire Génome et Développement des Plantes, Unité Mixte de Recherche 5096, 66860 Perpignan, France

ORCID IDs: 0000-0001-9389-2906 (R.M.-P.); 0000-0001-6929-8034 (R.S.-M.); 0000-0001-9410-6946 (S.F.-C.); 0000-0001-5571-0665 (A.C.-F.); 0000-0002-2717-7995 (J.S.-V.); 0000-0003-0770-4230 (M.R.P.)

Ribosome biogenesis is crucial for cellular metabolism and has important implications for disease and aging. Human (*Homo sapiens*) glioma tumor-suppressor candidate region gene2 (GLTSCR2) and yeast (*Saccharomyces cerevisiae*) Nucleolar protein53 (Nop53) are orthologous proteins with demonstrated roles as ribosome biogenesis factors; knockdown of GLTSCR2 impairs maturation of 18S and 5.8S ribosomal RNAs (rRNAs), and Nop53 is required for maturation of 5.8S and 25S rRNAs. Here, we characterized SMALL ORGAN4 (SMO4), the most likely ortholog of human GLTSCR2 and yeast Nop53 in Arabidopsis (*Arabidopsis thaliana*). Loss of function of SMO4 results in a mild morphological phenotype; however, we found that *smo4* mutants exhibit strong cytological and molecular phenotypes: nucleolar hypertrophy and disorganization, overaccumulation of 5.8S and 18S rRNA precursors, and an imbalanced 40S:60S ribosome subunit ratio. Like yeast Nop53 and human GLTSCR2, Arabidopsis SMO4 participates in 5.8S rRNA maturation. In yeast, Nop53 cooperates with mRNA transport4 (Mtr4) for 5.8S rRNA maturation. In Arabidopsis, we found that SMO4 plays similar roles in the 5.8S rRNA maturation pathway than those described for MTR4. However, SMO4 seems not to participate in the degradation of by-products derived from the 5′-external transcribed spacer (ETS) of 45S pre-rRNA, as MTR4 does.

The eukaryotic 80S cytoplasmic ribosome was first described in the mid-1950s (Palade, 1955) and is now considered a paradigm for our understanding of complex molecular machines (Dinman, 2009). The structure and biogenesis of the 80S ribosome are similar in all eukaryotes. The ribosomal RNAs (rRNAs) and ribosomal proteins (RPs) involved in these processes are also highly conserved. The function of the 80S ribosome in mRNA translation exhibits high-level evolutionary conservation, similar to that of other essential cellular functions (Wilson and Doudna Cate, 2012).

Approximately 80 RPs and four rRNAs form the 80S ribosome. These rRNAs are produced via processing of the primary transcripts of the repeated 5S ribosomal DNA (rDNA) genes in all eukaryotes, and 47S, 45S, and 35S rDNA genes in animals, plants, and yeast, respectively. The processing of the 5S pre-rRNA primary transcript to produce mature 5S rRNA is a straightforward process. By contrast, the processing of 47S/45S/35S pre-rRNA to produce mature 5.8S and 18S rRNAs in all eukaryotes, mature 25S rRNA in yeast and plants, and mature 28S rRNA in animals is a complex, multistep process (Supplemental Figs. S1–S3; Wilson and Doudna Cate, 2012). The biogenesis of the 80S ribosome in eukaryotes is best characterized in the yeast *Saccharomyces cerevisiae*. Indeed, the individual functions of many plant and animal ribosome biogenesis factors (RBFs) and their interactions have been inferred based on their homology with yeast putative orthologs (Tomecki et al., 2017; Sáez-Vásquez and Delseny, 2019).

The exosome, an evolutionarily conserved complex in eukaryotes, has 3′ to 5′ exoribonuclease activity,

[1]This work was supported by the Ministerio de Economía, Industria y Competitividad of Spain (grant nos. BIO2014–56889–R and BIO2017–89728–R to M.R.P.), the Generalitat Valenciana (grant no. PROMETEO/2019/117 to M.R.P.), and the Agence Nationale pour la Recherche (grant no. ANR–17–CE12–0026–01 to J.S.-V.).

[2]These authors contributed equally to the article.

[3]Present address: INRAE, Université de Bordeaux, UMR 1332 Biologie du Fruit et Pathologie, F–33882 Villenave d'Ornon cedex, France.

[4]Author for contact: mrponce@umh.es.

[5]Senior author.

The author responsible for distribution of materials integral to the findings presented in this article in accordance with the policy described in the Instructions for Authors (www.plantphysiol.org) is: María Rosa Ponce (mrponce@umh.es).

M.R.P. conceived and supervised the study, obtained funding, and provided resources; M.R.P., R.M.-P., and R.S.-M. designed the methodology; all authors performed the research and analyzed the data; M.R.P. and R.M.-P. wrote the original draft; all authors reviewed and edited the article.

[OPEN]Articles can be viewed without a subscription.

www.plantphysiol.org/cgi/doi/10.1104/pp.19.01540

which is required for the metabolism of many RNA species, such as mRNAs, rRNAs, small nucleolar RNAs, and small nuclear RNAs. The exosome facilitates the degradation, surveillance, precursor processing, and degradation of processing by-products of these RNA species (Kilchert et al., 2016). In yeast, Nucleolar protein53 (Nop53; Thomson and Tollervey, 2005) acts as an adaptor protein that targets the mRNA transport4 (Mtr4) ATP-dependent RNA helicase (Kilchert et al., 2016) to preribosomal particles for exosome processing of the 3′ end of the 7S pre-rRNA, a 5.8S rRNA precursor (Supplemental Fig. S1; Thoms et al., 2015). The loss of Nop53 function perturbs 5.8S and 25S rRNA biogenesis but not that of 18S rRNA, leading to severely stunted growth and an imbalance in the 40S:60S ribosomal subunit ratio (Granato et al., 2005; Sydorskyy et al., 2005; Thomson and Tollervey, 2005). Yeast Mtr4, also termed Dependent on eIF4B, is also essential; the loss of Mtr4 function reduces 5.8S rRNA production (de la Cruz et al., 1998).

Knockdown of human (*Homo sapiens*) *MTR4* leads to the strong accumulation of 34S pre-rRNA (an aberrant early precursor of 18S rRNA, produced by the inhibition of the cleavage at the A′, A_0, and 1 endonucleolytic sites; Supplemental Fig. S2) and the overaccumulation of 26S and 18S-E pre-rRNAs (late precursors of 18S rRNA; Supplemental Fig. S2; Tafforeau et al., 2013). Arabidopsis (*Arabidopsis thaliana*) *mtr4* mutants overaccumulate precursors of the 18S and 5.8S rRNAs, but the levels of the mature rRNAs are not affected in these mutants (Supplemental Fig. S3; Lange et al., 2011). The Arabidopsis ortholog of yeast Nop53 is encoded by AT2G40430, which was previously named *SMALL ORGAN4* (*SMO4*) by Zhang et al. (2015); these authors characterized SMO4 as a nuclear protein that affects cell proliferation. However, to date, a role for SMO4 in ribosome biogenesis has not been established.

The human ortholog of yeast Nop53 is the nucleolar protein glioma tumor-suppressor candidate region gene2 (GLTSCR2; Lee et al., 2012), which is also known as GSCR2, p60, and protein interacting with carboxyl terminus1 (PICT1). GLTSCR2 is an essential protein whose loss of function stabilizes p53 and induces p53-dependent G1 cell cycle arrest and apoptosis (Sasaki et al., 2011). GLTSCR2 is also considered to be a key regulator of p53-mediated responses to the nucleolar stress caused by impaired ribosomal biogenesis or function (Suzuki et al., 2012). Knockdown of *GLTSCR2* causes the overaccumulation of 47S pre-rRNA, the primary transcript of 47S rDNA genes, and of 18S-E pre-rRNA, a late intermediate of 18S rRNA maturation, as well as 12S pre-rRNA, a 5.8S rRNA precursor (Supplemental Fig. S2; Tafforeau et al., 2013).

In Arabidopsis, ARGONAUTE1 (AGO1) is the main RNase that functions in posttranscriptional gene silencing (PTGS) pathways mediated by microRNAs and other small RNAs (Baumberger and Baulcombe, 2005). We previously performed a second-site mutagenesis of *ago1-52* (which carries a hypomorphic and viable mutant of *AGO1*) and isolated 22 lines carrying extragenic suppressor mutations (Micol-Ponce et al., 2014). Several of these mutations were alleles of AT4G02720, which we named *MORPHOLOGY OF ARGONAUTE1-52 SUPPRESSED2* (*MAS2*); we found *MAS2* to be the ortholog of the gene encoding animal NF-κ-B-activating protein (NKAP; Micol-Ponce et al., 2014; Sánchez-García et al., 2015). In a yeast two-hybrid screen, we identified 14 MAS2 interactors (Sánchez-García et al., 2015), including SMO4 and RIBOSOMAL RNA PROCESSING7 (RRP7), an RBF that participates in 18S rRNA maturation (Micol-Ponce et al., 2018). MAS2 negatively regulates 45S rDNA expression (Sánchez-García et al., 2015).

Here, we investigated the action and interactions of Arabidopsis *SMO4*. The genetic interactions of *smo4* alleles found in this study confirm the functional relationship of *SMO4* with *MAS2* and *MTR4*. The morphological, cytological, and molecular phenotypes caused by the loss of function of *SMO4* shed light on the role of SMO4 in ribosome biogenesis, specifically in 5.8S rRNA maturation, as it has been shown for its yeast and human orthologs.

RESULTS

Nop53/GLTSCR2 Family Members Possess a Conserved Motif That Participates in the Interaction with the Exosome Cofactor Mtr4

The Arabidopsis Information Research 10 (TAIR10) and Araport11 annotations describe AT2G40430 (*SMO4*) as encoding a homolog of yeast Nop53. Compared with human GLTSCR2, yeast Nop53 and Arabidopsis SMO4 share 18.53% and 20.7% amino acid sequence identity and 30.76% and 35.2% similarity, respectively. Yeast Nop53 and Arabidopsis SMO4 share only 17.23% identity and 31.46% similarity. According to TAIR10, *SMO4* transcription generates three splice variants, which encode proteins with 442 (AT2G40430.1, encoding SMO4.1), 449 (AT2G40430.2, encoding SMO4.2), and 441 (AT2G40430.3, encoding SMO4.3) amino acids. The SMO4.2 protein harbors an extension of seven amino acids at its C terminus.

In yeast, an N-terminal LFXφD arch interaction motif (AIM; where X is any amino acid and φ is a hydrophobic amino acid) of Nop53 interacts with the arch domain of the exosome cofactor Mtr4 (Jackson et al., 2010; Thoms et al., 2015). The AIM in yeast Nop53, human GLTSCR2, and Arabidopsis SMO4 is well conserved, despite the relatively low shared identities between the full-length proteins. The AIM sequence of Arabidopsis SMO4 and yeast Nop53 is LFHVD, and that of human GLTSCR2 is LFFVD (where V is Val, a hydrophobic residue; Supplemental Fig. S4; Thoms et al., 2015). This motif is present in species representative of all major plant clades, as shown in a multiple sequence alignment of plant putative Nop53 orthologs, where φ is V except for soybean (*Glycine max*; which harbors E [Glu], a charged residue, at this position;

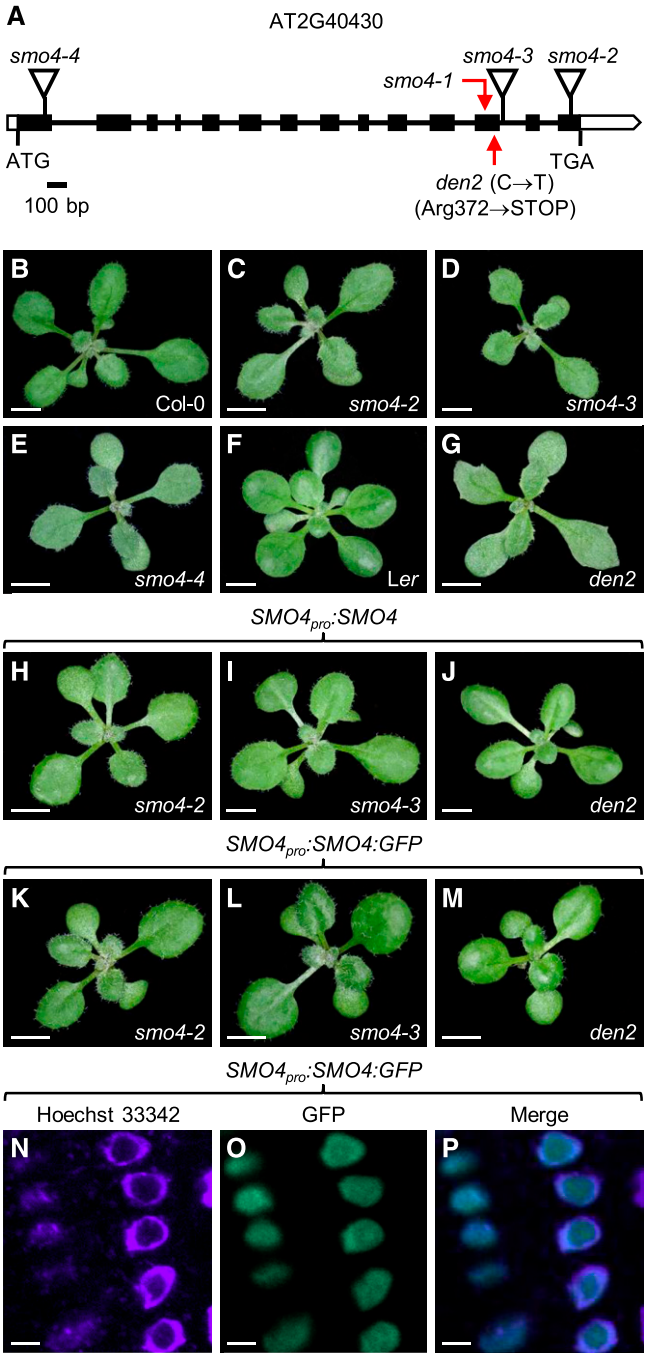

Figure 1. *SMO4* gene structure, rosette phenotypes and phenotypic rescue of *smo4* mutants, and subnuclear localization of the SMO4 protein. A, Schematic representation of *SMO4* gene structure including the molecular nature and positions of the mutations studied in this work. The *SMO4.2* (AT2G40430.2) gene model, which corresponds to the splice variant that is predicted to produce the largest SMO4 protein, is shown. The start (ATG) and stop (TGA) codon positions are also indicated. Black and white boxes represent exons and 5′ and 3′ untranslated regions, respectively. Lines between boxes represent introns, and triangles indicate T-DNA insertions. Red arrows indicate the positions of the 14-bp deletion of *smo4-1* and the single-base substitution of *den2*. B to M, Rosette morphological phenotypes of Col-0 (B), *smo4-2* (C), *smo4-3* (D), *smo4-4* (E), L*er* (F), *den2* (G), *smo4-2* $SMO4_{pro}$*:SMO4* (H), *smo4-3* $SMO4_{pro}$*:SMO4* (I), *den2* $SMO4_{pro}$*:SMO4* (J), *smo4-2* $SMO4_{pro}$*:SMO4:GFP* (K), *smo4-3* $SMO4_{pro}$*:SMO4:GFP* (L), and *den2* $SMO4_{pro}$*:SMO4:GFP* (M) plants. All plants were homozygous for the mutant alleles and the transgenes shown. Photographs were taken 14 das. Bars = 3 mm. N to P, Confocal laser-scanning micrographs of cells from the root elongation zone of plants homozygous for the $SMO4_{pro}$*:SMO4:GFP* transgene in the Col-0 background. Fluorescent signals correspond to Hoechst 33342 (N), GFP (O), and their overlay (P). Bars = 5 μm.

Supplemental Fig. S5). Arabidopsis MTR4 also contains an arch domain (Jackson et al., 2010; Lange et al., 2014). Mutational analysis in yeast has shown that the arch domain of Mtr4 is necessary for the 3′ processing of 7S pre-rRNA, to yield mature 5.8S rRNA, and in the degradation of the by-product of 5′-ETS (Supplemental Fig. S1; Jackson et al., 2010). The full-length MTR4 is more conserved than NOP53, including the arch domain, which is not the most highly conserved region among eukaryotic MTR4 proteins (Supplemental Figs. S6 and S7; Lange et al., 2014).

Isolation of Novel Alleles of *SMO4*

In yeast, the lack of *Nop53* function is lethal or associated with significant growth defects (Granato et al., 2005; Sydorskyy et al., 2005; Thomson and Tollervey, 2005). The *smo4-1* mutant, the first *smo4* mutant identified in Arabidopsis, was isolated based on its phenotype: reduced plant size resulting from delayed cell cycle progression during leaf development, which eventually reduces cell number (Zhang et al., 2015). The *smo4-1* allele carries a 14-bp deletion in the 12th exon of *SMO4* (Fig. 1A), which is predicted to produce a truncated protein 12 amino acids shorter than the wild-type version. In two insertional mutants, the transfer DNA (T-DNA) insertions disrupted *SMO4* in its 14th exon (*smo4-2*; SALK_012561; Zhang et al., 2015) and 12th intron (*smo4-3*; SALK_071764; Micol-Ponce et al., 2018; Fig. 1A). Under our growth conditions, *smo4-2* and *smo4-3* plants, observed 14 days after stratification (das), had very mild morphological phenotypes, with slightly dentate and pointed rosette leaves; these mutant plants were nearly indistinguishable from the wild type at bolting (Fig. 1, B–D). These *smo4* alleles might be hypomorphic, based on their weak mutant phenotypes and because the T-DNA insertions in *smo4-2* and *smo4-3* and the deletion mutation in *smo4-1* are located near the 3′ end of the AT2G40430 coding region (Fig. 1A). Hence, we also included in our study the GABI_082H04 line (hereafter referred to as *smo4-4*), which carries a *smo4* allele with a T-DNA insertion disrupting the first exon of *SMO4* (Fig. 1, A and E). Homozygous *smo4-2*, *smo4-3*, and *smo4-4* plants displayed indistinguishable phenotypes, suggesting that each mutant allele confers the same loss of function of *SMO4* and that they all are likely to be null.

In a large-scale ethyl methanesulfonate (EMS) mutant screening performed in the laboratory of José Luis Micol, 58 *denticulata* (*den*) pointed-leaf mutants were isolated and fell into 17 complementation groups (Berná et al., 1999). A single *den2* mutant allele was subsequently isolated and mapped at low resolution to chromosome 2 (Robles and Micol, 2001). Here, we delimited a 3.8 Mb genomic region candidate to harbor the *den2* mutation, using iterative linkage analysis to molecular markers (Supplemental Table S1), and performed whole-genome sequencing of DNA from *den2* plants. This analysis revealed a C→T base substitution in 12th exon of AT2G40430, which is placed within the candidate genomic region. This base change is predicted to be a nonsense mutation (Arg372→stop), producing a truncated protein 71 amino acids shorter than the wild-type protein (Fig. 1A), losing the most conserved region among yeast, human, and Arabidopsis NOP53 orthologs (Supplemental Fig. S4), which suggests that *den2* is a null allele of *SMO4*. A *smo4-3* × *den2* cross confirmed that these two mutants are allelic (Supplemental Fig. S8).

To further examine if the mutant alleles of *SMO4* under study are null, we used several primer pairs, each flanking one of the *smo4* insertions or hybridizing in the T-DNA and the *SMO4* gene, to perform semiquantitative reverse transcription PCR (RT-PCR) analyses of *smo4-2*, *smo4-3*, *smo4-4*, and *den2* transcription (Supplemental Fig. S9; Supplemental Table S2). We detected transcripts including exons located upstream of the insertions of *smo4-2* and *smo4-3*, and downstream of those of *smo4-3* and *smo4-4* (Supplemental Fig. S9B). Our results for *smo4-2* are in accordance with those obtained by Zhang et al. (2015). In addition, we obtained bands with sizes that may correspond to chimeric transcripts, including T-DNA and *SMO4* sequences, in all *smo4* mutants (Supplemental Fig. S9B). Since these alleles cause almost identical phenotypes and are predicted to produce aberrant proteins, irrespective of the positions of the mutations at the beginning (the *smo4-4* insertion) or the end (the *smo4-2* and *smo4-3* insertions and the *den2* point mutation) of the coding region, we concluded that probably all of them carry null alleles of *SMO4*. The morphological phenotype of *den2* (Fig. 1, F and G) is stronger than those of the *smo4* mutants (Fig. 1, C–E); this is likely to be due to the Landsberg *erecta* (L*er*) genetic background of *den2*, as already shown for other mutants, including mutants affected in genes related to ribosome biogenesis (Horiguchi et al., 2011; Rosado et al., 2012).

To confirm that the mutant phenotypes of *smo4* and *den2* are caused by a lack of *SMO4* activity, we created the $SMO4_{pro}$:*SMO4* construct, which was transferred into *smo4-2*, *smo4-3*, *den2*, Columbia-0 (Col-0), and L*er* plants. The $SMO4_{pro}$:*SMO4* transgene complemented the mutant phenotypes caused by the *smo4* and *den2* mutations (Fig. 1, H–J). We also created the $35S_{pro}$:*SMO4* construct, which had no visible morphological effects when transferred into the Col-0 and L*er* wild types (Supplemental Fig. S10).

SMO4 Localizes to the Nucleolus and Nucleoplasm

In addition to 5.8S rRNA maturation (Supplemental Fig. S1), yeast Nop53 is required for the nuclear export of the 60S preribosomal particle, which matures in the cytoplasm into the 60S subunit of the 80S ribosome (Thomson and Tollervey, 2005). To play this dual role in ribosome biogenesis, we reasoned that SMO4 must be present in both the nucleolus and nucleoplasm, similar to yeast Nop53 (Sydorskyy et al., 2005; Thomson and Tollervey, 2005). To test this hypothesis, we generated the $SMO4_{pro}$:*SMO4*:*GFP* construct, which produced a functional protein that complemented the mutant phenotypes of *smo4-2*, *smo4-3*, and *den2* (Fig. 1, K–M). SMO4 is a nuclear protein (Zhang et al., 2015), but whether it localizes to the nucleolus and/or nucleoplasm is unknown. To visualize the nucleus, we stained the roots of Col-0 $SMO4_{pro}$:*SMO4*:*GFP* plants with Hoechst 33342, a dye that strongly binds to double-stranded DNA but not to RNA, the primary nucleic acid in the nucleolus. GFP fluorescence was detected in a diffuse pattern in the nucleolus and nucleoplasm (Fig. 1, N–P). In agreement with these findings, SMO4 has also been identified in the nucleolar proteome of Arabidopsis (Montacié et al., 2017).

smo4-3 Genetically Interacts with *mtr4-2*, *mas2-1*, and *parallel1-2*

RRP7 and SMO4 were found as interactors of MAS2 (the NKAP ortholog in Arabidopsis) in yeast two-hybrid assays (Sánchez-García et al., 2015). RRP7 is involved in 18S rRNA maturation, and its complete lack of function in the *rrp7-1* and *rrp7-2* insertional mutants causes a strong pointed-leaf phenotype. To establish the functional relationship between RRP7 and SMO4, we obtained the *smo4-3 rrp7-1* double mutant, which was indistinguishable from *rrp7-1*, suggesting that *rrp7-1* is epistatic to *smo4-3* (Micol-Ponce et al., 2018). The *mas2-1* mutation was isolated by its dominant suppressor effect on the morphological phenotype of *ago1-52* but lacks phenotypic effects by itself as a single mutant (Fig. 2, A and B; Sánchez-García et al., 2015). However, the presence of *mas2-1* causes a synergistic effect on the morphological phenotype of *rrp7-1*: *rrp7-1 mas2-1* double mutant seedlings develop pointed cotyledons and very dwarf rosettes with extremely narrow leaves. These results genetically confirm the functional relationship between *RRP7* and *SMO4* and between *RRP7* and *MAS2* (Micol-Ponce et al., 2018).

To ascertain if *SMO4* genetically interacts with *MTR4* and *MAS2*, we crossed *smo4-3* to *mtr4-2* and *mas2-1* (Fig. 2, B, C, and G). We also crossed *smo4-3* to mutants carrying alleles of the paralogous Arabidopsis genes *NUC1* and *NUC2* (encoding NUCLEOLIN), which antagonistically act in the control of 45S rDNA transcription (Pontvianne et al., 2007; Durut et al., 2014). *NUC1* is expressed in all tissues, and its mutations cause nucleolar disorganization, chromatin decondensation at

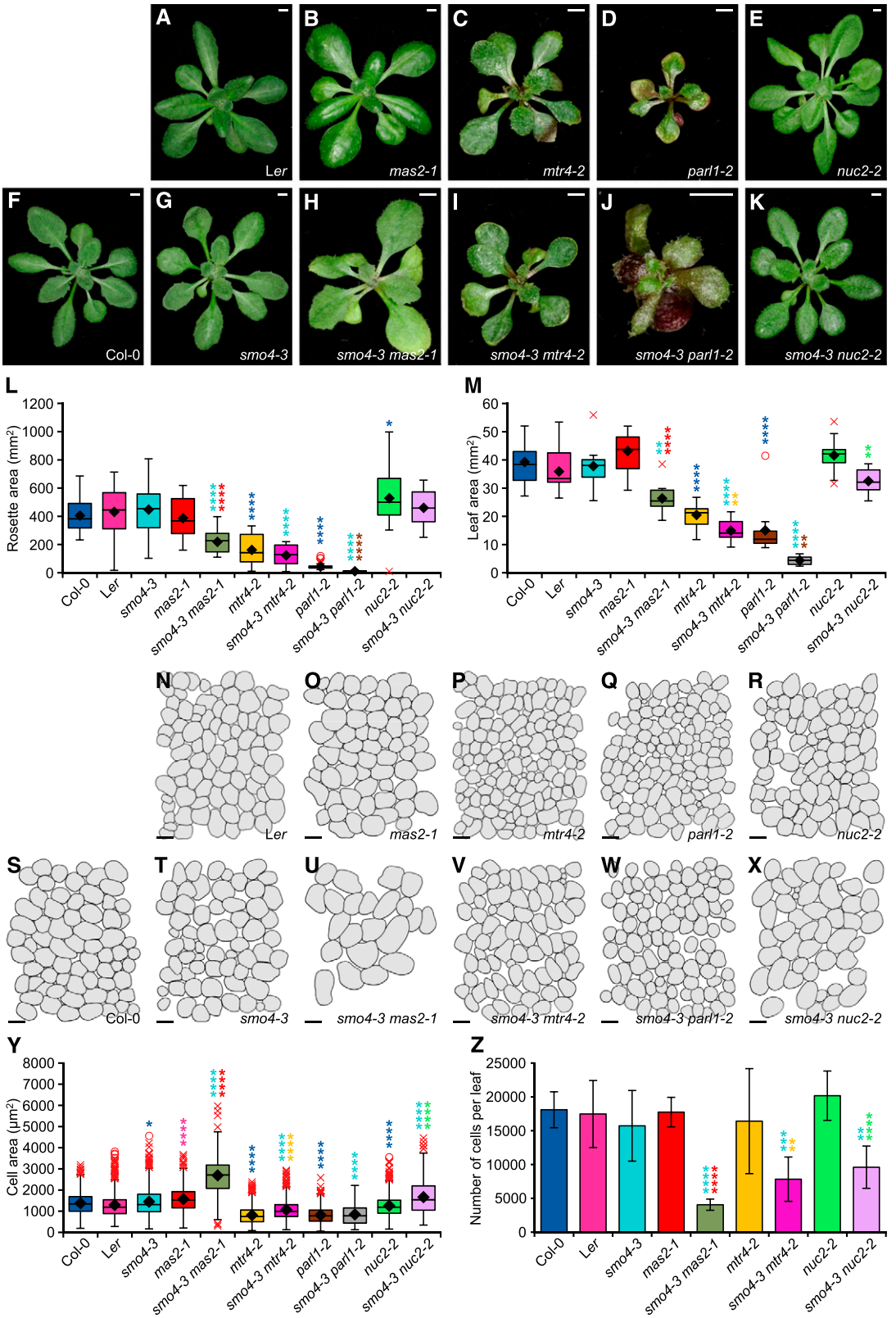

Figure 2. Genetic interactions of *smo4-3* with *mas2-1*, *mtr4-2*, *parl1-2*, and *nuc2-2*. A to K, Rosettes of L*er* (A), *mas2-1* (B), *mtr4-2* (C), *parl1-2* (D), *nuc2-2* (E), Col-0 (F), *smo4-3* (G), *smo4-3 mas2-1* (H), *smo4-3 mtr4-2* (I), *smo4-3 parl1-2* (J), and *smo4-3 nuc2-2* (K) plants. Photographs were taken 21 das. Bars = 2 mm. L and M, Box plots showing the distribution of rosette (L) and leaf (M) areas in plants of the genotypes shown. Boxes are delimited by the first (Q1; bottom hinge) and third (Q3; top hinge) quartiles.

the nucleolar organizer regions, and the up-regulation of 45S rDNA. *NUC2* is expressed at much lower levels than *NUC1* in wild-type plants but is induced in the *nuc1* mutant background (Durut et al., 2014). *NUC1* loss of function causes aberrant leaf development and vein patterning. This phenotype was described for the null alleles of *NUC1* named *parallel1* (*parl1*; Fig. 2D); *parl1* mutants accumulate $35S_{A123B}$ pre-rRNA due to failed cleavage at the P site (Petricka and Nelson, 2007; Pontvianne et al., 2007) of the 5′-ETS of the $35S_{A123B}$ pre-rRNA (Supplemental Fig. S3). The only effects of mutations in *NUC2* on the morphological phenotype are an increased rosette size and mild late flowering (Fig. 2E; Durut et al., 2014).

The *smo4-3 mtr4-2*, *smo4-3 mas2-1*, and *smo4-3 parl1-2* double mutants, but not *smo4-3 nuc2-2*, were smaller than *smo4-3* (Fig. 2, H–L). In addition, *smo4-3 mas2-1* plants displayed a synergistic phenotype, showing markedly dentate, pale leaves with reduced chlorophyll levels compared with the mutant parental lines and the wild type (Fig. 2, B and F–H; Supplemental Fig. S11A). Anthocyanin levels and rosette size were similar in *smo4-3 mtr4-2* and *mtr4-2* (Fig. 2, C and I; Supplemental Fig. S11B). The *smo4-3 parl1-2* plants exhibited narrow leaves and very small rosettes (Fig. 2J). Leaf lamina and whole rosette areas in *smo4-3* were similar to those of Col-0, as expected, but were reduced in most of the double mutants (Fig. 2, L and M). However, rosette size was similar in *smo4-3 nuc2-2* and *smo4-3* plants (Fig. 2, G, K, and L), even though *nuc2-2* rosettes were larger than Col-0 rosettes (Fig. 2, E, F, and L). These results reinforce the notion that *SMO4* promotes leaf growth (Zhang et al., 2015).

Palisade mesophyll cell size increases in the *smo4* mutants (Zhang et al., 2015), and leaf venation is aberrant in *parl1* mutants (Petricka and Nelson, 2007). We performed a morphometric analysis of these phenotypes (Fig. 2, M–Z) and found that palisade mesophyll cells were larger in *smo4-3* than in Col-0 (Fig. 2, S, T, and Y), but to a lesser extent than that previously described (Zhang et al., 2015), perhaps due to differences in culture conditions and/or the node chosen for study. Palisade mesophyll cells were also enlarged in *mas2-1* compared with L*er* (Fig. 2, N, O, and Y), but were smaller in *mtr4-2* and much smaller in *parl1-2*, compared with Col-0 (Fig. 2, P, Q, S, and Y). *mas2-1* and *nuc2-2* double mutant combinations with *smo4-3* exhibited increased palisade mesophyll cell size, particularly *smo4-3 mas2-1* (Fig. 2, O, R, T, U, X, and Y). These results indicate that the reduction of leaf and rosette area in these double mutants is caused by decreased cell proliferation but not cell expansion. This hypothesis is supported by the finding that the number of palisade mesophyll cells per leaf was much lower in the double mutants than in the single mutants (Fig. 2Z). We did not obtain results from *parl1-2* or *smo4-3 parl1-2* leaves, except for the cellular area (Fig. 2, W and Y), as they became extremely fragile after depigmentation treatment. In line with these findings, the use of the $SMO4_{pro}$:*GUS* transgene revealed the strongest expression of *SMO4* in proliferating tissues (Supplemental Fig. S12), as previously described (Zhang et al., 2015).

We detected similar alterations in leaf venation patterns in *mtr4-2* and *parl1-2* plants compared with Col-0 but not in *smo4-3*, *mas2-1*, and *nuc2-2* (Supplemental Fig. S11, D–I; Supplemental Table S3), which correspond to the stronger morphological phenotypes of *mtr4-2* and *parl1-2*. *parl1-2* leaves exhibit aberrant venation patterns (Petricka and Nelson, 2007), as do *mtr4-2* cotyledons (Lange et al., 2011). The most aberrant venation pattern that we found in double mutants was that of *smo4-3 parl1-2*, which showed the lowest values of venation length, branching, and density (Supplemental Fig. S11L; Supplemental Table S4). These results reveal the synergistic effect of the *smo4-3 parl1-2* genetic combination. The leaf venation pattern of *smo4-3 mtr4-2* was more similar to that of *mtr4-2* than to *smo4-3*, as also observed for leaf and rosette morphology (Supplemental Fig. S11, E, I, and K).

smo4 Mutants Show Defects in 18S and 5.8S rRNA Maturation

As mentioned above, yeast Mtr4 and Arabidopsis MTR4 interact with the nuclear exosome for 5.8S rRNA maturation, and yeast Nop53 acts as an adaptor protein for this interaction (Lange et al., 2011, 2014; Thoms et al., 2015). In Arabidopsis *mtr4* plants, unprocessed 18S and 5.8S rRNAs, as well as 5′-ETS by-products (downstream of the P site), overaccumulate (Lange et al., 2011). To visualize the intermediates of 45S pre-rRNA processing (Supplemental Fig. S3), we performed gel-blot analyses of RNA extracted from *smo4-2*, *smo4-3*, and *den2* plants using the previously described S2, S7, and S9 probes, which are complementary to a

Figure 2. (*Continued.*)
Whiskers represent Q1 − 1.5 × IQR (bottom) and Q3 + 1.5 × IQR (top), where the interquartile range (IQR) is Q3 − Q1. Black diamonds = means; black lines = medians; red crosses = outliers; and red circles = extreme minimum (less than Q1 − 3 × IQR) or maximum (greater than Q3 + 3 × IQR) outliers. Asterisks indicate values significantly different from the corresponding wild-type or parental line (indicated by color) by Student's *t* test (*$P < 0.05$; **$P < 0.01$; and ****$P < 0.0001$). More than 20 rosettes and 10 first-node leaves collected 21 das were analyzed per genotype. N to X, Diagrams of the subepidermal layer of palisade mesophyll cells from first-node leaves collected 21 das. Bars = 40 μm. Y, Box plot showing the distribution of cell sizes in the subepidermal layer of palisade mesophyll cells from first-node leaves. Z, Number of palisade mesophyll cells of the subepidermal layer per leaf. Ten leaves collected 21 das were studied per genotype in Y and Z, and more than 230 cells were analyzed per genotype in Y. Error bars indicate SD. Asterisks indicate values significantly different from the corresponding wild-type or single-mutant parental line (indicated by color) by Student's *t* test (*$P < 0.05$; **$P < 0.01$; ***$P < 0.001$; and ****$P < 0.0001$).

segment of the 5′-ETS, internal transcribed spacer 1 (ITS1), and ITS2, respectively (Fig. 3A; Lange et al., 2011).

Using the S9 probe, we detected similar levels of 5.8S rRNA precursors (pre-5.8S) in *smo4* mutants, which were markedly higher than in Col-0, L*er*, and *smo4-3 SMO4*$_{pro}$*:SMO4* (Fig. 3B; Supplemental Fig. S3; Supplemental Table S5). Precursors of 5.8S rRNA, including the 7S (5.8S + 120 nucleotides), 5.8S+70, and 6S (5.8S + 11/12 nucleotides) pre-rRNAs, accumulated in these mutants, whereas they were nearly or completely undetectable in L*er*, Col-0, and *smo4-3 SMO4*$_{pro}$*:SMO4* plants (Fig. 3, B and C; Supplemental Fig. S3). These precursors of 5.8S rRNA also accumulate at similar levels in *mtr4* mutants, as previously described (Lange et al., 2011), and more strongly in *smo4-3 mtr4-2* double mutants compared with *mtr4-2* and *smo4-3* (Fig. 4, A and B; Supplemental Tables S5 and S6).

Using the S7 probe, accumulation of P-A_3 pre-rRNA, the first 18S rRNA precursor in the ITS1-first pathway, was detected in *smo4* mutants, to a lesser extent than the 5.8S pre-rRNAs, but not in *smo4-3 SMO4*$_{pro}$*:SMO4* and *mtr4-2* plants (Fig. 3E; Supplemental Fig. S3; Supplemental Table S5). As previously reported (Lange et al., 2011), we detected the accumulation of P′-A_3 in *mtr4-2*, as in *den2*, but not in the other *smo4* mutants (Fig. 3E; Supplemental Table S5). P′-A_3 is generated by cleavage at the P′ site of the P-A_3 pre-rRNA or at the A_3 site of the 33S(P′) pre-rRNA (Supplemental Fig. S3). In *mtr4* mutants, the levels of the 18S rRNA remained unaltered, but the P′-A_3 and 18S-A_3 pre-rRNAs, which are polyadenylated, accumulated, indicating that these

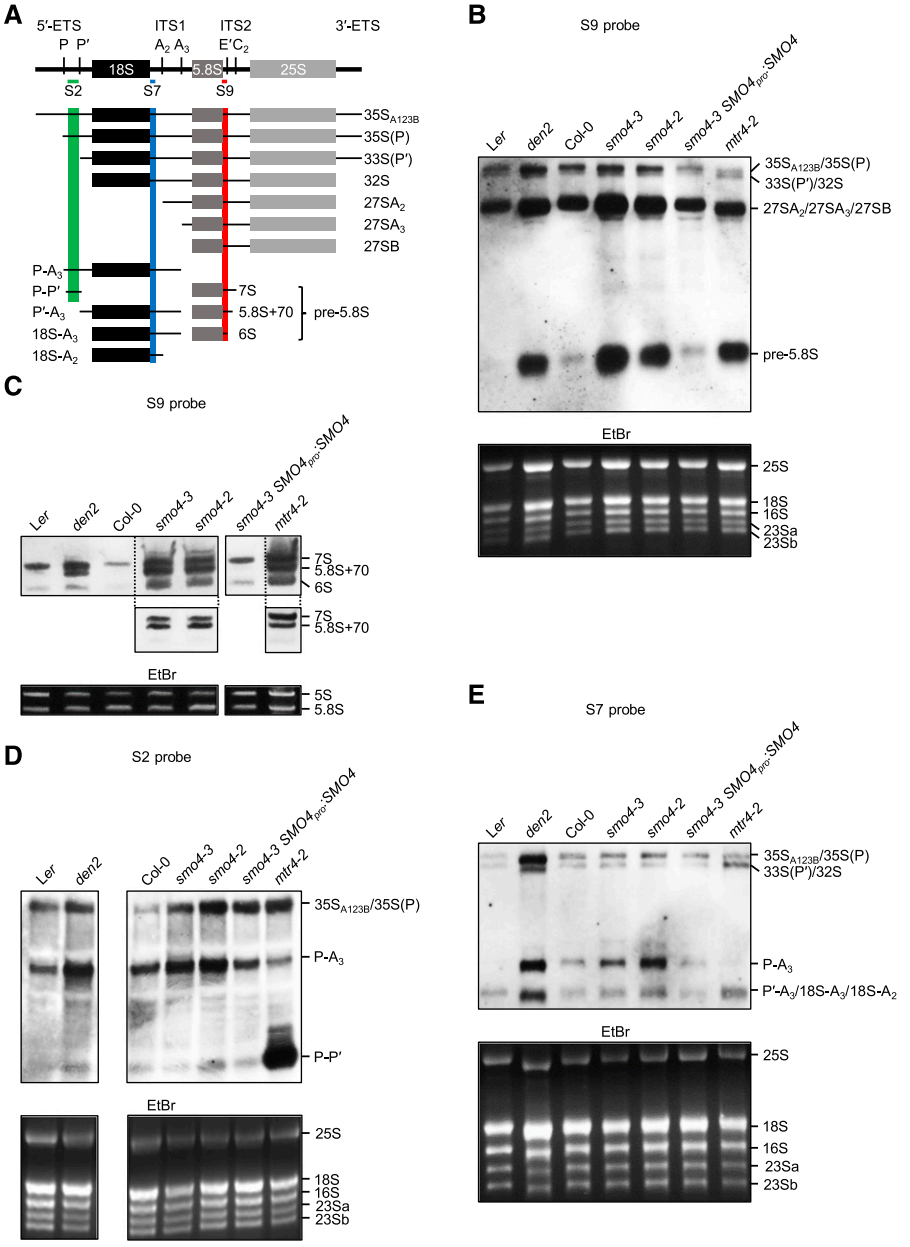

Figure 3. Visualization by RNA gel blots of 45S pre-rRNA processing in the *smo4-2*, *smo4-3*, *den2*, and *mtr4-2* single mutants. A, Diagram (modified from Hang et al. [2014]) illustrating the pre-rRNA processing intermediates that can be detected in RNA gel blots using the S2, S7, or S9 probes. The precursor regions hybridizing with the probes are highlighted in green (S2 probe), blue (S7), and red (S9). Vertical bars indicate the endonucleolytic cleavage sites relevant to this study (P, P′, A_2, A_3, E′, and C_2). B to E, Visualization of the processing of 5.8S (B and C) and 18S (D and E) rRNA precursors using RNA gel blots. Total RNA was separated on formaldehyde-agarose (B, D, and E) or polyacrylamide-urea (C) gels, transferred to a nylon membrane, and hybridized with the S9 (B and C), S2 (D), or S7 (E) probe. Two views of the bands visualized from *smo4-3*, *smo4-2*, and *mtr4-2* RNA with the S9 probe are provided in C, one of which corresponds to a very short exposure time, which allowed 7S and 5.8S+70 pre-rRNAs to be distinguished. EtBr, Ethidium bromide-stained gels, visualized before blotting, which served as loading controls. Similar results were obtained in at least two independent experiments. Relative quantification of the bands visualized with the S9, S7, and S2 probes is shown in Supplemental Table S5.

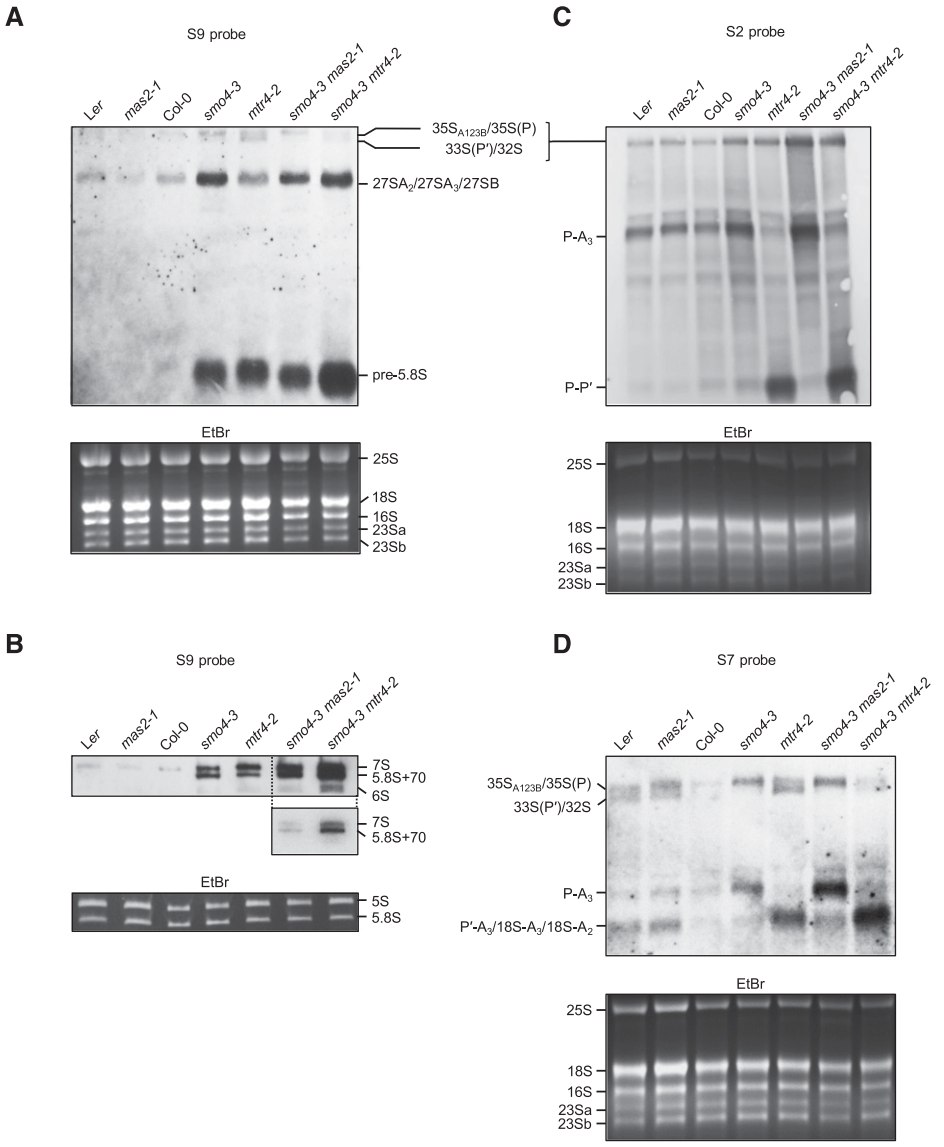

Figure 4. Visualization by RNA gel blots of 45S pre-rRNA processing in the *smo4-3 mas2-1* and *smo4-3 mtr4-2* double mutants. RNA gel blots using the S9 (A and B), S2 (C), and S7 (D) probes are shown. Total RNA was separated on formaldehyde-agarose (A, C, and D) and polyacrylamide-urea (B) gels, transferred to a nylon membrane, and hybridized with the corresponding probe. Two views of the bands visualized from *smo4-3 mtr4-2* RNA with the S9 probe are provided in B, one of which corresponds to a very short exposure time, which allowed 7S and 5.8S+70 pre-rRNAs to be distinguished. EtBr, Ethidium bromide-stained gels, visualized before blotting, which served as loading controls. Similar results to those shown here were obtained in at least two independent experiments. Relative quantification of the bands visualized with the S9, S7, and S2 probes from *smo4-3 mtr4-2* RNA is shown in Supplemental Table S6.

pre-rRNAs are targets of the exonucleolytic activity of the exosome. The P′-A_3 and 18S-A_3 pre-rRNAs could be by-products of an irregular processing of the 18S rRNA precursors at their 3′ end (Lange et al., 2011). The differential accumulation of 18S rRNA precursors, such as P-A_3 in *smo4*, and P′-A_3 and 18S-A_3 in *mtr4-2*, was confirmed in three RNA gel blots performed using the S7 probe, in each one of which a different biological replicate per genotype was used. Using the r5 + r6, r5 + r7, and r5 + r8 primer sets for circular RT-PCR analyses, we obtained bands of the same sizes than those previously described (Hang et al., 2014; Liu et al., 2016), which corresponded to the P-A_3, P′-A_3, 18S-A_2, 18S-A_3, 33S, 32S, and 27SA_2 precursors, as we confirmed by Sanger sequencing (Fig. 5; Supplemental Table S7). These circular RT-PCR results reconfirmed our findings on the differential accumulation of the P-A_3 pre-rRNA in the *smo4* mutants.

To ascertain if the accumulation of the P-A_3 pre-rRNA in the *smo4* mutants is caused by defective processing, we cloned the products that we obtained by circular RT-PCR using the r5 + r6 primer set (Fig. 5A). Sanger sequencing of these molecules showed that their 5′ and 3′ extremities (29 clones were analyzed from Col-0 and 27 from *smo4-3*) corresponded to the correct processing at the P and A_3 endonucleolytic sites and that the polyadenylation status of their 3′ ends was similar for both genotypes (Supplemental Fig. S13). Polyadenylation of pre-rRNAs occurs mainly after cleavage and stimulates its exonucleolytic trimming by the exosome (Slomovic et al., 2006). Our results suggest that SMO4 is not required for the correct cleavage and polyadenylation of the P-A_3 pre-rRNA. However, the observed P-A_3 pre-rRNA accumulation suggests its delayed 5′ end processing at the P′ site. These results are in agreement with the existence of a mechanism of quality control to ensure a balanced synthesis of the 40S and 60S ribosomal subunits,

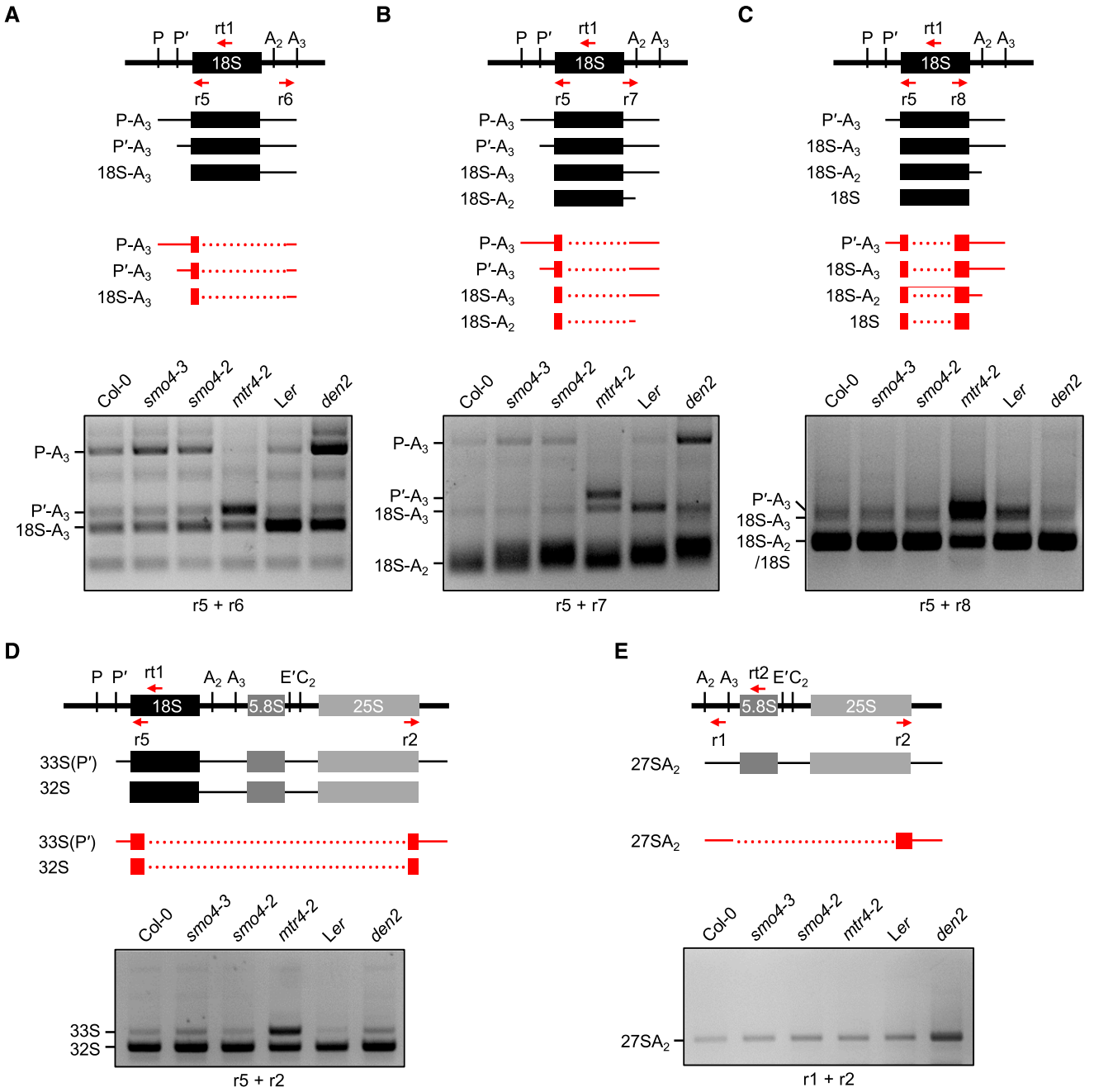

Figure 5. Visualization by circular RT-PCR amplification of 45S pre-rRNA processing in the *smo4-2*, *smo4-3*, *den2*, and *mtr4-2* mutants. Ethidium bromide-stained agarose gels visualizing products from the circular RT-PCR amplifications performed are shown. RNA was extracted and circularized with T4 RNA ligase and reverse transcribed using the rt1 (A–D) or rt2 (E) primer, and the resulting cDNA was PCR amplified with the r5 + r6 (A), r5 + r7 (B), r5 + r8 (C), r5 + r2 (D), and r1 + r2 (E) primer pairs. The full names of the rt1 and rt2 primers were 18c and 5.8SrRNA_R, respectively. Diagrams illustrate all (D) or part (A–C and E) of the 45S pre-rRNA, represented in black and gray (see Fig. 3A), with indication of the positions of the primers used for circular RT-PCR amplifications. Circular RT-PCR products are shown in red. Given that the primers used are divergent, part of the cDNA obtained from each circularized rRNA precursor (dotted red lines) is absent from the final circular RT-PCR products.

as previously proposed for *mtr4* mutants (Lange et al., 2011), which show an inefficient 5.8S rRNA maturation, as *smo4* mutants do.

Using the S2 probe, we detected in *mtr4-2* plants strong accumulation of the P-P′ fragment (Fig. 3D; Supplemental Table S5), a by-product generated by the early processing of the 5′-ETS 45S pre-rRNA, or the P-A_3 precursor of the 18S rRNA, as previously described (Lange et al., 2011). The overaccumulation of the P-P′ by-product was similar between *smo4-3 mtr4-2*

and *mtr4-2* (Fig. 4C; Supplemental Table S6), whereas the levels in wild-type plants, *smo4-2*, *smo4-3*, *den2*, and *smo4-3 SMO4$_{pro}$:SMO4* were similar (Fig. 3D; Supplemental Table S5).

Taken together, these results indicate that MTR4 and SMO4 act together in 5.8S rRNA but that SMO4 does not participate in the degradation of by-products derived from the 5′-ETS, as MTR4 does (Lange et al., 2011).

18S and 5.8S pre-rRNA Species Accumulate in the Nucleoli of *smo4* Plants

Given that 45S pre-rRNA processing is defective in *smo4-2*, *smo4-3*, and *den2* plants, we investigated whether any mature or precursor rRNA species accumulate in the nucleolus or nucleoplasm in these mutant lines. We first performed RNA fluorescence in situ hybridization (RNA-FISH) using the S9 and S2 probes, which hybridize with the 5.8S and 18S pre-rRNAs, respectively, but not with their corresponding mature rRNAs (Fig. 3A). We detected fluorescence mainly in the nucleolus for both wild types and mutant lines, but with high differences in intensities among them (Fig. 6, A–D1). Using the S9 probe, we observed increased fluorescence in *smo4-3* nucleoli (1.46-fold compared with Col-0), *den2* (1.59-fold compared with L*er*), and *mtr4-2* (1.32-fold compared with Col-0; Fig. 6E1). Such increases were much less pronounced than the accumulation of the pre-5.8S rRNA species that we observed in RNA gel blots (Fig. 3, B and C; Supplemental Table S5). These results suggest that immature 5.8S rRNAs are incorporated to the 60S subunit and exported to the cytoplasm.

With the S2 probe, we found higher fluorescence levels relative to the wild types in *smo4-3* (2.13-fold) and *den2* (1.64-fold), which accumulate the P-A_3 pre-rRNA, and in *mtr4-2* (2.59-fold), which accumulates the P-P′ by-product (Fig. 6F1; Supplemental Table S5). These results suggest that these two RNA species, P-A_3 and P-P′, are retained within the nucleolus, and that they are the major contributors to the high fluorescence level detected with the S2 probe in *smo4* and *mtr4-2* mutants, respectively. It is worth mentioning here that relative fluorescence levels are underestimated in the mutants, mainly those of *den2*, because the detector of the confocal microscope was saturated for many dots. Saturation was unavoidable because of the extreme differences in fluorescence intensities between the *smo4* and *mtr4-2* mutants and their corresponding wild types; raising the level of detection resulted in undetectable signals from the wild types.

Our RNA-FISH experiments revealed hypertrophy of the nucleolus in *smo4* mutants but not in *mtr4-2*, and it was particularly pronounced in *den2* (Fig. 6). Then, we quantified the nucleolar and nuclear areas in Col-0, L*er*, *smo4-3*, and *den2* plants. To delimitate the nucleolus, we carried out immunolocalizations using an antibody against the nucleolar marker fibrillarin, and stained the samples with DAPI to visualize the nucleoplasm (Fig. 7, A–L). Both the nucleoplasm and nucleolus were larger in *smo4-3* and *den2* than in Col-0 or L*er*, especially the nucleolus (Fig. 7, M–P). These quantitative results confirm the notion that the loss of SMO4 activity causes nucleolar hypertrophy. In addition, fibrillarin exhibited nonuniform staining in Col-0 and L*er*, which was more diffuse and with a more granular appearance in *smo4-3* and *den2* (Fig. 7, A–L), pointing to some degree of disorganization of the nucleolus.

Ribosome Profiles Are Slightly Imbalanced in *smo4* Plants

Finally, to evaluate whether ribosome assembly was impaired in the *smo4* mutants, we obtained ribosome profiles of Col-0, *smo4-2*, *smo4-3*, and *smo4-3 SMO4$_{pro}$:SMO4* seedlings. Specifically, we fractionated purified cell extracts through sucrose gradients to separate the 40S and 60S ribosomal subunits, the 80S monosome, the 90S preribosome, and polysomes. We did not observe major defects in the 60S and 80S peaks, but the 40S particle overaccumulated in both mutants, which was normalized in *smo4-3 SMO4$_{pro}$:SMO4* plants (Fig. 8), according to its wild-type phenotype (Fig. 1I). An excess of the 40S subunit has also been found in yeast cells lacking Nop53 activity, which causes an imbalanced 40S:60S ratio (Sydorskyy et al., 2005). In addition, we detected a peak corresponding to particles that sedimented slightly more rapidly than 80S monosomes, which might have been 90S particles (Fig. 8). The nature of the peak that sedimented more slowly than 40S particles is unknown. Neither of these peaks showed major changes in the mutants compared with Col-0 and served as internal controls.

DISCUSSION

Evolutionary Conservation and Divergence of SMO4 Function in Ribosome Biogenesis

80S ribosome biogenesis is an essential, evolutionarily conserved process that has diverged among fungi, plants, and animals. The extent of this conservation is demonstrated by the existence of one or more Arabidopsis orthologs for 179 of the approximately 250 RBFs in yeast (Simm et al., 2015). Evidence of the divergence in 80S ribosome biogenesis is provided by the observations that many human orthologs of yeast RBFs are involved in pre-rRNA processing but have evolved different functions and that 74 human RBFs lack orthologs in yeast (Wild et al., 2010; Tafforeau et al., 2013).

Based on their homology with yeast and human proteins, several hundred Arabidopsis proteins are annotated as encoding putative components of the ribosome biogenesis machinery, including RPs and RBFs (Sáez-Vásquez and Delseny, 2019). Mutants

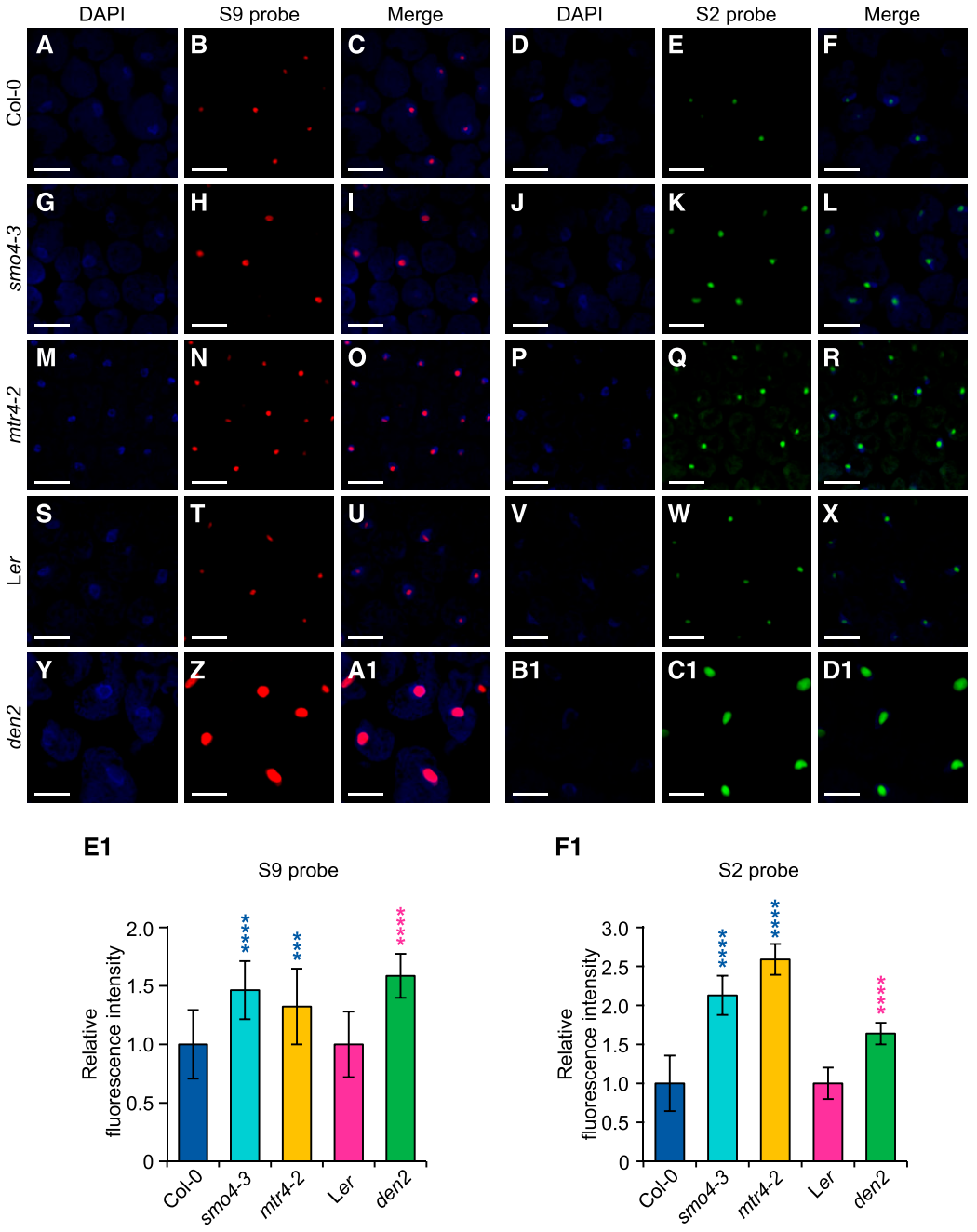

Figure 6. Subcellular localization of 5.8S and 18S rRNA precursors in the *smo4-3*, *den2*, and *mtr4-2* mutants. A to D1, RNA-FISH assays in palisade mesophyll cells from first-node leaves of Col-0 (A–F), *smo4-3* (G–L), *mtr4-2* (M–R), L*er* (S–X), and *den2* (Y–D1). Fluorescent signals correspond to 4′,6-diamidino-2-phenylindole (DAPI; A, D, G, J, M, P, S, V, Y, and B1), which was used as a nuclear marker (in blue); S9 probe labeled with Cy3 (in red; B, H, N, T, and Z); S2 probe labeled with FAM (in green; E, K, Q, W, and C1); and the overlay of the previous signals (C, F, I, L, O, R, U, X, A1, and D1). Photographs were taken from plants collected 14 das. Bars = 25 μm. E1 and F1, Relative fluorescence intensity from the S9 (E1) and S2 (F1) probes, measured in 10 nuclei per leaf from six leaves per genotype. Error bars indicate SD. Asterisks indicate values significantly different from the corresponding wild type (indicated by color) by Student's *t* test (***$P < 0.001$ and ****$P < 0.0001$).

representing more than 20 mutated RP-encoding genes have been isolated in screens for morphological aberrations or embryonic lethality (Byrne, 2009; Horiguchi et al., 2011). A recent survey of plant RBFs at the mutational and molecular levels revealed 28 individual proteins, 27 of which have yeast orthologs. For all but two of these plant RBFs, gene mutations result in developmental defects, and mutants in 16 of

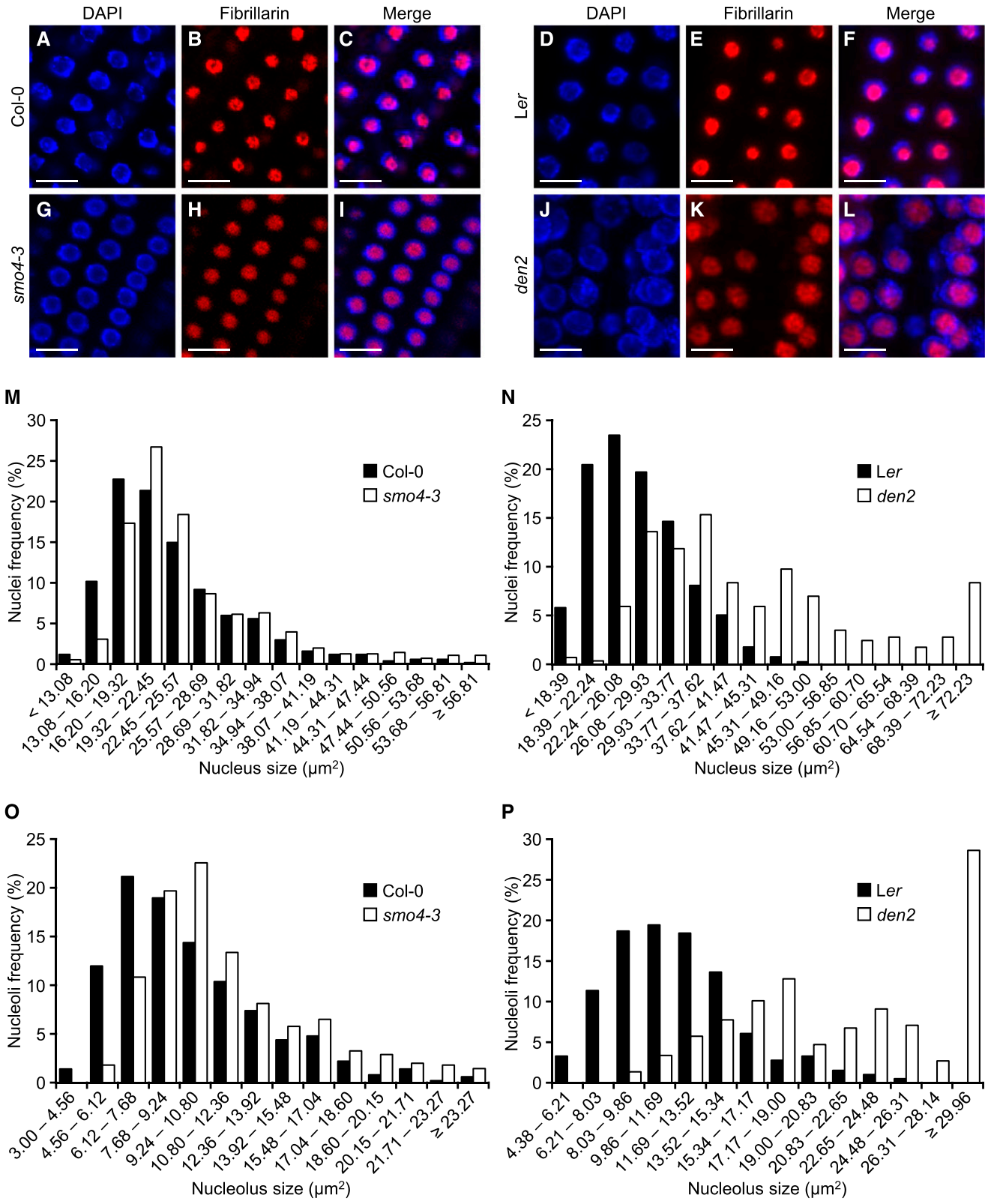

Figure 7. Quantification of nucleolar size in root cells of *smo4-3* and *den2* mutants. A to L, Visualization by immunolocalization of the fibrillarin nucleolar marker in Col-0 (A–C), L*er* (D–F), *smo4-3* (G–I), and *den2* (J–L) plants. Fluorescent signals correspond to DAPI (A, D, G, and J), the secondary antibody for fibrillarin detection (B, E, H, and K), and their overlay (C, F, I, and L). Bars = 10 μm. M to P, Distribution of the sizes of nuclei (M and N) and nucleoli (O and P) of the *smo4-3* and *den2* mutants and their

these RBF-encoding genes overaccumulate pre-rRNAs, indicating that rRNA maturation is defective. The wild-type versions of 18 of these Arabidopsis RBF-encoding genes have been transferred into yeast strains, carrying mutations causing the absence or depletion of the corresponding RBF ortholog; however, no complementation of the yeast RBF mutant phenotype was observed for 10 of the 18 Arabidopsis RBF-encoding genes examined (Weis et al., 2015); one of these Arabidopsis RBF-encoding genes is *MTR4*, which did not complement *mtr4* mutations in yeast (Lange et al., 2014). It is thus not surprising that Arabidopsis *SMO4* did not complement a *Nop53* lack-of-function mutation in yeast (Zhang et al., 2015).

Our results provide experimental evidence for the role of SMO4 as an RBF in 45S pre-rRNA processing. Indeed, in the *smo4* and *den2* mutants, we detected accumulation of three 5.8S rRNA precursors that were nearly absent in wild-type and *smo4-3 SMO4*$_{pro}$:*SMO4* plants: the 7S (5.8S + 120 nucleotides), 5.8S+70, and 6S (5.8S + 11/12 nucleotides) pre-rRNAs (Fig. 3, B and C; Supplemental Table S5). These mutants also accumulated P-A_3 pre-rRNA, an 18S rRNA precursor that is only produced by the ITS1-first pathway. In addition, *den2* accumulates all rRNA precursors that we have detected in RNA blots, including the P′-A_3 pre-rRNA, which also accumulates in *mtr4* mutants (Fig. 3E; Supplemental Fig. S3; Supplemental Table S5). These results suggest that the processing of the 45S pre-rRNA is delayed in *smo4* mutants.

Yeast *Nop53* is a single-copy, essential gene, as is expected from its key role in rRNA maturation (Granato et al., 2005). *SMO4* is also a single-copy gene in Arabidopsis, and previous studies with two *smo4* alleles, including *smo4-2*, have shown that *SMO4* is required but not essential for cell cycle progression and survival (Zhang et al., 2015). Our work with two additional insertional alleles, and *den2*, which does not produce a full-length protein, suggests that the absence of SMO4 causes mild morphological phenotypes that become less apparent during later stages of plant development (Zhang et al., 2015; this work). In fact, as previously noted (Zhang et al., 2015), the C-terminal region of the wild-type SMO4 protein, which is predicted to be absent from the DEN2 protein, is the most conserved part among yeast, human, and Arabidopsis orthologs (Supplemental Fig. S4).

We have observed a dramatic hypertrophy of the nucleolus in *smo4* mutants, mainly in the *den2* mutant, as well as disorganization of the nucleolus, revealed by an atypical distribution of fibrillarin. Morphometric analysis of *smo4* mutants has shown that SMO4 positively regulates cell proliferation (Zhang et al., 2015; this study). It is possible that, similar to GLTSCR2, SMO4 participates in the control of the progression of the cell cycle in response to nucleolar stress.

SMO4 and *MAS2* Are Functionally Related

The number of proteins known to bind to RNA or to participate in processes involving RNA molecules has increased over the past decades, together with the number of known RNA functions. Some of these proteins play multiple roles in RNA metabolism pathways, many of which appear to be ancient. For example, metazoan NKAPs are multifunctional factors involved in the regulation of diverse processes, such as cellular differentiation, proliferation, and apoptosis. Human NKAP immunoprecipitates together with several RBFs, most of which are involved in 18S rRNA maturation, and it can associate with different spliceosomal complexes and to premRNAs and spliced mRNAs as well as to small nuclear RNAs, small nucleolar RNAs, rRNAs, and long intergenic noncoding RNAs (Burgute et al., 2014).

Small RNAs are involved in PTGS pathways and the epigenetic regulation of gene transcription. To further explore the role of AGO1, the main RNase that functions in PTGS pathways mediated by microRNAs, we previously performed a screen for suppressors of the morphological phenotype of the *ago1-52* hypomorphic and viable allele (Micol-Ponce et al., 2014). One suppressor gene that we identified was *MAS2*, but the *mas2* alleles that we isolated, which were dominant and likely antimorphic, act as informational suppressor mutations (Sánchez-García et al., 2015). Comparable to its NKAP orthologs, MAS2 is essential and multifunctional, acting in processes such as splicing and ribosome biogenesis. In a search for physical interactors of MAS2, we identified two RBFs, RRP7 (Micol-Ponce et al., 2018) and SMO4 (this work), as well as RPS24B (encoded by AT5G28060), an RP whose yeast and human orthologs also act as RBFs for 18S rRNA maturation (Ferreira-Cerca et al., 2005; Choesmel et al., 2008). The *SMO4*, *RRP7*, and *MAS2* promoters share regulatory motifs that are enriched in genes encoding factors involved in translation, including RBFs (Micol-Ponce et al., 2018). The epistatic interaction of *rrp7-1* on *smo4-3* found in *smo4-3 rrp7-1* plants and the synergistic phenotypes of the *rrp7-1 mas2-1* (Micol-Ponce et al., 2018) and *smo4-3 mas2-1* (this work) double mutants indicate that *SMO4*, *RRP7*, and *MAS2* are functionally related. We did not detect alterations in 45S pre-rRNA processing in *mas2-1* plants or in the *smo4-3 mas2-1* double mutant, which was the same as that in *smo4-3* (Fig. 4), indicating that the synergistic effect in the double mutants was not due to the role of SMO4 in 45S pre-rRNA processing.

Figure 7. (*Continued.*)
corresponding wild types. Between 287 and 554 cells were studied per genotype, from the roots of five seedlings of each genotype, collected 5 das. Nuclei and nucleoli size distributions of *smo4-3* and *den2* were significantly different from the corresponding wild type in a Kolmogorov-Smirnov test ($P < 0.0001$).

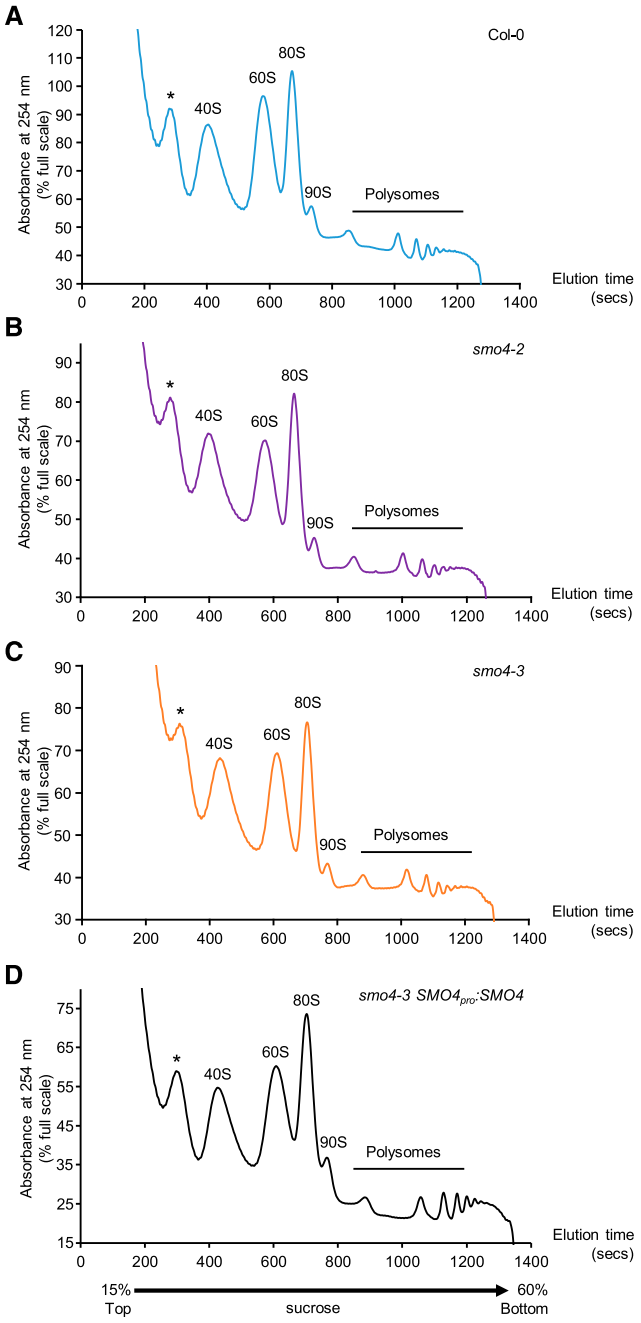

Figure 8. Ribosome profiles of the *smo4* mutants. Extracts from the aerial organs of wild-type (A), *smo4-2* (B), *smo4-3* (C), and *smo4-3 SMO4*$_{pro}$*:SMO4* (D) plants were collected 18 das and then lysed and fractionated through 15% to 60% sucrose gradients by ultracentrifugation. The percentage of the full scale of absorbance was monitored at 254 nm. Peaks corresponding to 40S and 60S ribosomal subunits, 80S monosomes, 90S preribosome, and polysomes are indicated. The asterisks indicate an unknown particle.

We have not yet identified in silico yeast orthologs of Arabidopsis MAS2 or human NKAP. However, *Dictyostelium discoideum* has an NKAP ortholog that also appears to be a multifunctional protein that coimmunoprecipitates with several RPs and RNA-binding proteins, including RBFs such as bystin (Burgute et al., 2016). *S. cerevisiae* possesses a bystin ortholog named Essential nuclear protein1 (Enp1), which is required for efficient nuclear export of the pre-40S ribosomal particle (Seiser et al., 2006). In the *enp1* and *mtr4* yeast mutants, mRNAs are retained within the nucleolus. Nuclear retention of mRNAs is also caused by mutations in genes involved in rRNA biogenesis or premRNA splicing, ribosome quality control (including genes encoding components of the nuclear exosome), and mRNA nuclear export (Paul and Montpetit, 2016).

SMO4 Is Functionally Related to *MTR4* and *NUC1*

Yeast Nop53 acts as an adaptor protein that interacts with the arch domain of Mtr4 via its AIM for the recruitment of exosomes to rRNA precursors (Thoms et al., 2015). Notwithstanding the low level of similarity observed between SMO4 and its yeast Nop53 and human GLTSCR2 orthologs, the AIM in these proteins is conserved, as in comparable proteins in many other plant species (Supplemental Figs. S4 and S5). The conservation of the SMO4 AIM and the MTR4 arch domain in Arabidopsis and other plant species (Supplemental Fig. S7) suggests that the mechanism of exosome recruitment to 45S pre-rRNA is also conserved in the plant kingdom. Taken together, these findings and the similar morphological phenotypes of *mtr4-2*, *smo4-2*, *smo4-3*, and *den2* plants indicate that MTR4 and SMO4 play related roles in the 45S pre-rRNA processing pathways.

Most bands that we visualized in RNA blots using the S9 probe were similar in size and intensity in *smo4-3*, *smo4-2*, and *den2*, as well as in *mtr4-2* and the *smo4-3 mtr4-2* double mutant. These results suggest that SMO4 facilitates the exonucleolytic trimming of 5.8S rRNA precursors, a process comparable to that of yeast Mtr4 and Arabidopsis MTR4 in *mtr4* plants (Lange et al., 2011). However, unlike MTR4, SMO4 seems to not participate in the degradation of by-products of the early steps of 45S pre-rRNA processing, suggesting that MTR4 associates with other protein(s). Two partners of yeast Mtr4 have been identified: Nop53 and U three protein18 (Utp18), a component of the small subunit processome, a large ribonucleoprotein complex that participates cotranscriptionally in early 35S pre-rRNA processing, to generate pre-18S rRNA (Phipps et al., 2011). Interactions between Mtr4 and both Nop53 and Utp18 are required to recruit the exosome to the precursors of 5.8S rRNA and 5′-ETS, respectively (Bernstein et al., 2004; Falk et al., 2017). Utp18 orthologs, including Arabidopsis UTP18 (encoded by AT5G14050), harbor the conserved AIM (Thoms et al., 2015), suggesting that Arabidopsis UTP18 could be a second partner of MTR4, required for 5′-ETS degradation. However, SMO4 and UTP18 were not identified among the proteins that copurified with MTR4-GFP (Lange et al., 2014), perhaps because

they do not interact or because the GFP tail in the fusion protein prevented their interaction.

The weak morphological phenotypes of *smo4* mutants and their ribosomal profiles suggest that mature, functional 18S and 5.8S rRNAs are produced in these plants, as has been observed in *mtr4* mutants, suggesting that ribosome biogenesis is delayed. It also appears that the overaccumulation of 5.8S and 18S rRNA precursors in the *smo4* and *den2* mutants has no effect on viability or fertility and only mildly affects development. The synergistic phenotype of *smo4-3 parl1-2* provides genetic evidence for the functional relationship between SMO4 and NUC1, both of which function as RBFs in 45S pre-rRNA processing.

Based on the morphological phenotype of the double mutants generated in this study, *mtr4-2* appears to be epistatic to *smo4-3*, since rosettes were indistinguishable between *smo4-3 mtr4-2* and *mtr4-2*, but clearly different from that of *smo4-3* (Fig. 2, C, G, and I). *mtr4-2* leaves are more pointed than those of *smo4-3*, and *mtr4-2* rosettes are smaller than those of *smo4-3* (Fig. 2, C, G, and L; Supplemental Table S3). These findings are consistent with the results of our molecular analysis of 45S pre-rRNA processing in the single and double mutants, indicating that both MTR4 and SMO4 act together in 5.8S rRNA maturation. In addition, our analysis using the S2 probe showed that MTR4 but not SMO4 participates in the degradation of 5′-ETS byproducts of 45S pre-rRNA processing.

MATERIALS AND METHODS

Plant Materials and Growth Conditions

Arabidopsis (*Arabidopsis thaliana*) L*er* and Col-0 wild-type accessions were obtained from the Nottingham Arabidopsis Stock Centre and propagated in the laboratory for further analysis. Seeds of the *smo4-2* (SALK_012561; Zhang et al., 2015), *smo4-3* (SALK_071764; Micol-Ponce et al., 2018), *smo4-4* (GABI_082H04; this work), *parl1-2* (SALK_002764; Petricka and Nelson, 2007), *nuc2-2* (GABI_178D01; Durut et al., 2014), and *mtr4-2* (SAIL_50_C11; Lange et al., 2011) lines were also provided by the Nottingham Arabidopsis Stock Centre. Each of these mutants carries a T-DNA insertion in the Col-0 genetic background. The *den2* and *mas2-1* mutants were isolated in the L*er* background after EMS mutagenesis performed in the laboratories of José Luis Micol (Berná et al., 1999) and M.R.P. (Micol-Ponce et al., 2014), respectively.

Seed sterilization and sowing, plant culture, and crosses were performed as previously described (Ponce et al., 1998; Berná et al., 1999), except for plants used for ribosome profiling (see below). When required, culture media were supplemented with hygromycin (15 μg mL^{-1}).

Molecular Characterization of Mutations

To characterize *den2*, a candidate interval of 3,827 kb was delimited by iterative linkage analysis as previously described (Ponce et al., 1999, 2006) using PCR amplification and the polymorphic markers listed in Supplemental Table S1. The *den2* point mutation was ultimately identified by whole-genome, next-generation sequencing, looking for the transitions typically caused by EMS (G→A or C→T) within the candidate interval. Only one EMS-type mutation (G→A) was found in a coding region and verified by Sanger sequencing. The raw data have been deposited in the Sequence Read Archive (https://www.ncbi.nlm.nih.gov/sra/) database under accession number SRP103180.

The presence of T-DNA insertions in the *SMO4*, *NUC1*, *NUC2*, and *MTR4* genes was verified by PCR using the primers shown in Supplemental Table S2. Discrimination between the wild-type *MAS2* and mutant *mas2-1* alleles was carried out by PCR amplification followed by restriction analysis, as described by Sánchez-García et al. (2015).

For massive sequencing, DNA was extracted from plants using a DNeasy Plant Mini Kit (Qiagen), and sequencing was performed using the Ion Proton platform following the manufacturer's instructions (Applied Biosystems, now Thermo Fisher Scientific). The resulting reads were mapped to the TAIR10 version of the Col-0 reference genome with Torrent Suit Software v5.2.1 (Thermo Fisher Scientific), which was also used to compile a list of the mutations identified. Sanger sequencing was performed with ABI PRISM BigDye Terminator Cycle Sequencing kits on an ABI PRISM 3130xl Genetic Analyzer (Applied Biosystems).

Construction and Analysis of Transgenes and Transgenic Lines

Constructs for Gateway cloning were generated and transferred into plants as described by Sánchez-García et al. (2015). The pGEM-T Easy221 entry vector and the pMDC32, pMDC83, pMDC107, and pMDC164 destination vectors (Curtis and Grossniklaus, 2003) were used. Inserts were generated by PCR using primers that included *attB1* and *attB2* sequences, as detailed in Supplemental Table S2. Chemically competent *Escherichia coli* DH5α cells were transformed with BP or LR Gateway cloning reaction products using the heat shock method. *Agrobacterium tumefaciens* C58C1 cells carrying the pSOUP helper plasmid were transformed with the constructs by electroporation.

To obtain the $35S_{pro}$:*SMO4* and $35S_{pro}$:*SMO4*:*GFP* overexpression constructs, the full-length coding sequence (stop codons were removed to obtain all *GFP* translational fusions) was PCR amplified from Col-0. The 1,317-bp region upstream of the translation start codon of *SMO4* was PCR amplified and used as the promoter driving the $SMO4_{pro}$:*GUS* transgene. This same promoter region was present at one end of the 4,156-bp segment amplified to isolate the entire 2,839-bp *SMO4* transcription unit, which was used to create the $SMO4_{pro}$:*SMO4* and $SMO4_{pro}$:*SMO4*:*GFP* constructs. The fidelity of all constructs was verified by Sanger sequencing before they were transferred into plants via the floral dip method (Clough and Bent, 1998).

The subcellular localization of SMO4 was visualized in the roots of plants in the Col-0 background carrying the $SMO4_{pro}$:*SMO4*:*GFP* or $35S_{pro}$:*SMO4*:*GFP* transgene, with plant tissue collected 10 das. GUS activity was analyzed in homozygous plants, and photographs of three plants were taken from each of three independent lines per genotype.

Plant Morphometry, Histology, and Microscopy

Photographs of Arabidopsis plants were taken with a Nikon SMZ1500 stereomicroscope equipped with a Nikon DXM1200F digital camera. To obtain high-resolution images from large rosettes, four to five partial photographs from the same plant were taken and assembled using the Photomerge tool of Adobe Photoshop CS3 software. Some empty spaces resulting from the assembly were further equalized with the black background, using Adobe Photoshop CS3. Measurement of rosette sizes was performed 21 das with the NIS Elements AR 3.1 image-analysis package (Nikon) from photographs of plants in petri dishes taken with a Canon PowerShot S315 camera.

For morphometric analysis of leaf lamina, palisade mesophyll cells, and vein patterns, the ImageJ processing program (https://imagej.net/ImageJ), the NIS Elements AR 3.1 (Nikon) image-analysis package, and the phenoVein software (http://www.plant-image-analysis.org/) were used, respectively, as described previously (Robles et al., 2010; Pérez-Pérez et al., 2011). In brief, fully expanded first-node leaves were collected 21 das, cleared with ethanol and chloral hydrate, and mounted on slides. Micrographs of the internal tissues were obtained using a Leica DMRB microscope equipped with a Nikon DXM1200 digital camera. Diagrams of the palisade mesophyll cells and leaf venation patterns were drawn on the screen of a Cintiq 18SX Interactive Pen Display (Wacom) using Adobe Photoshop CS3 software.

All fluorescence and confocal laser-scanning microscopy images were generated using a D-Eclipse C1 confocal microscope equipped with a DS-Ri1 camera and digitally processed with EZ-C1 operation software (Nikon), with band-pass filters. For observing DAPI and Hoechst 33342 nuclear staining, laser excitation was carried out at 408 nm and their emissions collected at 450/35 nm. GFP and FAM were excited at 488 nm and their emissions collected at 515/30 nm. Tetramethylrhodamine-5-isothiocyanate and Cy3 (Cyanine 3) were excited at 544 nm and their emissions detected at 605/75 nm.

Chlorophyll and Anthocyanin Extraction and Measurements

To quantify chlorophyll and anthocyanin content, 30 and 10 independent biological replicates were used, respectively. Each biological replicate included three rosettes collected 18 das, which were pooled, weighed, and homogenized in a MixerMill 400 (Retsch) automatic mixer. Chlorophylls were extracted with cold 80% (v/v) acetone for 30 min in the dark with agitation. Cell debris was removed by centrifugation at 3,000 rpm for 15 min at 4°C, and the pigment concentration in the supernatant was spectrophotometrically determined as described by Arnon (1949). Anthocyanins were extracted in 45% (v/v) methanol and 5% (v/v) acetic acid buffer, and the samples were centrifuged twice for 5 min at 12,000 rpm to remove cellular debris. Pigment concentration in the supernatant was spectrophotometrically measured as described by Mancinelli (1990).

Semiquantitative RT-PCR, RNA Gel-Blot Analysis, and Circular RT-PCR Assays

Total RNA was extracted from the aerial tissues of plants collected 15 das using TRI RNA Isolation Reagent (Sigma-Aldrich). Each biological sample contained RNA extracted from three plants, each grown on a different plate.

For semiquantitative RT-PCR experiments, retrotranscription was carried out with random hexamer primers and Maxima Reverse Transcriptase (Invitrogen), following indications of the manufacturer. RNA was treated with Turbo DNase (Invitrogen) prior to the reverse transcription step. The *ACTIN2* (*ACT2*) housekeeping gene was used as an internal control. Sequences of primers for PCR amplifications of *ACT2* and *SMO4* cDNAs are indicated in Supplemental Table S2.

For RNA gel-blot analysis, 3 μg of total RNA was used per gel blot, and the samples were loaded onto 1.2% (w/v) agarose/formaldehyde or 6% (w/v) polyacrylamide (a ratio between acrylamide and bisacrylamide of 29:1)/8 M urea gels. The polyacrylamide gel was run for 1 to 3 h at 180 V in 0.5× Tris-borate/EDTA buffer. RNA was visualized following ethidium bromide staining and transferred and cross-linked onto a Hybond N^+ nylon membrane (Thermo Fisher Scientific). Hybridization and detection were carried out as previously described (Micol-Ponce et al., 2018) using digoxigenin-labeled probes and Lumi-Film Chemiluminescent Detection Films (Roche), which were exposed for 20 min, 1 h, or overnight. The S2 probe was synthetized by PCR using digoxigenin-11-dUTP, genomic DNA as template, and the S2 fw and S2 rev primers; the S7 and S9 probes were 5′ end digoxigenin-labeled oligonucleotides; these probes were synthetized by Eurofins Genomics. The sequences of the primers and oligonucleotides used to obtain all probes are described in Supplemental Table S7 and were taken from Lange et al. (2011). To compare band intensities between samples, film images were quantified by densitometry with the Vision-Capt software (Vilber Lourmat) using as an internal loading control the 18S rRNA band visualized with ethidium bromide.

Circular RT-PCR was performed as described by Hang et al. (2014) and Micol-Ponce et al. (2018) using the primers described in Supplemental Table S7. In short, 5 μg of total RNA was circularized with T4 RNA ligase and reverse transcribed with Maxima Reverse Transcriptase (Thermo Fisher Scientific) and the rt1 or rt2 primers (Supplemental Table S7). cDNA was amplified using the r5 primer combined with r2, r6, r7, or r8 or with the r1 + r2 primer set (Supplemental Table S7). Products corresponding to P-A_3 pre-rRNA obtained from Col-0 and *smo4-3* with the r5 + r6 primer set were gel excised, purified, and cloned into the pCR2.1 vector (Invitrogen), and several clones were sequenced using the M13F universal primer. The remaining products obtained with the r5 primer combined with r2, r6, r7, or r8 were not cloned; instead, they were gel excised, purified, and sequenced using the r5 primer.

RNA-FISH and Immunolocalization

RNA-FISH was carried out as described by Parry et al. (2006). Oligonucleotides, which were synthetized and labeled at their 5′ ends (Supplemental Table S7) by Eurofins Genomics, were used as probes. The S2 probe was labeled with FAM and the S9 probe with Cy3. Approximately 100 cells per genotype from the first-node leaves of 10 plants collected 14 das were analyzed and were fixed in glass vials at 600 mbar for 25 min. Probes were used in a 0.5 μg mL^{-1} hybridization solution. The samples were mounted on slides with a drop of Vectashield antifade mounting medium (Vector Laboratories) containing 0.01 μg mL^{-1} DAPI. Fluorescence intensity was measured with the EZ-C1 3.90 FreeViewer software (Nikon).

Immunolocalization was carried out as described by Pasternak et al. (2015). The assays were performed on 24-well microplates using the roots of seedlings collected 5 das. Samples were fixed for 40 min at 37°C with a solution containing 2% (v/v) paraformaldehyde in 1× microtubule-stabilizing buffer (50 mM PIPES, 5 mM $MgSO_4$, and 5 mM EGTA, pH 6.9) and 0.1% (v/v) Triton X-100. A 1:250 dilution of the mouse monoclonal primary anti-fibrillarin antibody [38F3] (Abcam) and a 1:500 dilution of the tetramethylrhodamine-5-isothiocyanate-conjugated anti-mouse IgG secondary antibody (Sigma-Aldrich) was used. Nuclei were stained for 10 min with 0.2 μg mL^{-1} DAPI and washed for 5 min before mounting the samples on slides.

To quantify nuclei and nucleoli sizes, their outlines were drawn from confocal images on a Wacom DTF-720 Pen Display using Adobe Photoshop CS3 software. Nuclei and nucleoli areas were measured from these diagrams with the NIS Elements AR 3.1 (Nikon) image-analysis package. The ratio between the areas of nuclei and nucleoli was obtained from 287 to 554 cells from five seedlings per genotype. The number of nuclei and nucleoli, which were classified into 16 and 14 groups, respectively, depending on their size, were determined and their percentages calculated. Statistical analysis of the distribution of nuclei and nucleoli areas was performed with the XLSTAT statistical software (Addinsoft).

Ribosome Profiling

Seeds were sown on petri dishes containing 1× Murashige and Skoog medium supplemented with 1% (w/v) sucrose and stratified for 2 d. Plants were grown under a 16-h-light (120 μE m^{-2} s^{-1})/8-h-dark cycle, at 21°C for 18 d, and relative humidity of 55% in light or 60% at night. Aboveground organs were collected 18 das, shock frozen in liquid nitrogen, and ground to a fine powder. Each 250-mg sample was resuspended in 750 μL of extraction buffer (0.2 M Tris-HCl, pH 9, 0.2 M KCl, 0.035 M $MgCl_2$, and 0.025 M EGTA, pH 8) supplemented with 1% (w/v) sodium deoxycholate, 1% detergent mix (5 g of Brij-35, 5 mL of Triton X-100, 5 mL of Igepal, and 5 mL of Tween 20), 2% (v/v) polyoxyethylene (10) tridecyl ether, 5 mM DTT reducing agent, 10 μM MG132 proteasome inhibitor, 50 μg mL^{-1} chloramphenicol, 100 μg mL^{-1} cycloheximide, and 100 μL of protease inhibitor cocktail for plant cell and tissue extracts (Sigma-Aldrich) per 10 mL of buffer. After 10 min of incubation on ice, the samples were centrifuged at 17,000*g* for 10 min at 4°C and the supernatant clarified through a 0.45-μm filter.

For ribosome profiling, 360 μL of clarified supernatant was layered onto a 9-mL linear 15% to 60% (w/v) sucrose gradient. After centrifugation in a Beckman SW41 rotor at 38,000 rpm for 3 h at 4°C, the gradient was analyzed using the Type 11 Optical Unit (Teledyne ISCO) attached to a UA-6 UV/VIS Detector (Teledyne ISCO) for continuous measurement of the A_{254}. The assay was repeated up to three times with consistent results.

Accession Numbers

We used *SMO4* as the name for AT2G40430 (Zhang et al., 2015), *MTR4* for AT1G59760 (Lange et al., 2011), *NUC1* or *PARL1* for AT1G48920 (Petricka and Nelson, 2007; Pontvianne et al., 2007), *NUC2* for AT3G18610 (Durut et al., 2014), *RRP7* for AT5G38720 (Micol-Ponce et al., 2018), and *MAS2* for AT4G02720 (Sánchez-García et al., 2015). Although several names have been used in the literature or databases for AT1G48920 and AT3G18610, we preferentially used the names *NUC1* and *NUC2* for these genes, respectively, throughout the article for simplicity.

Supplemental Data

The following supplemental materials are available.

Supplemental Figure S1. Overview of 35S pre-rRNA processing in yeast.

Supplemental Figure S2. Overview of 47S pre-rRNA processing in humans.

Supplemental Figure S3. Overview of 45S pre-rRNA processing in Arabidopsis.

Supplemental Figure S4. Sequence conservation among putative SMO4 orthologs in Arabidopsis, humans, and yeast.

Supplemental Figure S5. Sequence conservation among putative plant SMO4 orthologs.

Supplemental Figure S6. Sequence conservation among MTR4 orthologs in Arabidopsis, humans, and yeast.

Supplemental Figure S7. Sequence conservation among plant MTR4 orthologs.

Supplemental Figure S8. Allelism test of the *smo4-3* and *den2* mutants.

Supplemental Figure S9. Molecular effects of the *smo4* and *den2* mutations on the expression of the *SMO4* gene.

Supplemental Figure S10. Morphological and molecular effects of the expression of the $35S_{pro}$:*SMO4* transgene in the Col-0 background.

Supplemental Figure S11. Pigment concentration and leaf venation pattern in the double mutants studied in this work.

Supplemental Figure S12. *SMO4* gene spatial expression pattern.

Supplemental Figure S13. Sequences of the extremities of P-A_3 pre-rRNA molecules found in Col-0 and *smo4-3* RNA.

Supplemental Table S1. Primer sets used for the fine-mapping of *den2*.

Supplemental Table S2. Primer sets used in this work.

Supplemental Table S3. Morphometry of first-node leaf venation in the single mutants studied in this work.

Supplemental Table S4. Morphometry of first-node leaf venation in the double mutants studied in this work.

Supplemental Table S5. Relative quantification of several bands visualized with the S9, S7, and S2 probes in the RNA blots shown in Figure 3.

Supplemental Table S6. Relative quantification of several bands visualized with the S9, S7, and S2 probes in the RNA blots shown in Figure 4.

Supplemental Table S7. DNA probes and primers used for rRNA analysis.

ACKNOWLEDGMENTS

We thank José Manuel Serrano-García, Juan Castelló-Bañuls, and María José Ñíguez-Gómez for their excellent technical assistance and Amani Toumi for help in the preliminary analysis of *den2*. We also thank José Luis Micol for useful discussions, comments on the article, providing the *den2* mutant, and the use of his facilities.

Received December 16, 2019; accepted August 27, 2020; published September 10, 2020.

LITERATURE CITED

Arnon DI (1949) Copper enzymes in isolated chloroplasts: Polyphenoloxidase in *Beta vulgaris*. Plant Physiol **24:** 1–15

Baumberger N, Baulcombe DC (2005) Arabidopsis ARGONAUTE1 is an RNA Slicer that selectively recruits microRNAs and short interfering RNAs. Proc Natl Acad Sci USA **102:** 11928–11933

Berná G, Robles P, Micol JL (1999) A mutational analysis of leaf morphogenesis in *Arabidopsis thaliana*. Genetics **152:** 729–742

Bernstein KA, Gallagher JE, Mitchell BM, Granneman S, Baserga SJ (2004) The small-subunit processome is a ribosome assembly intermediate. Eukaryot Cell **3:** 1619–1626

Burgute BD, Peche VS, Müller R, Matthias J, Gaßen B, Eichinger L, Glöckner G, Noegel AA (2016) The C-terminal SynMuv/DdDUF926 domain regulates the function of the N-terminal domain of DdNKAP. PLoS ONE **11:** e0168617

Burgute BD, Peche VS, Steckelberg AL, Glöckner G, Gaßen B, Gehring NH, Noegel AA (2014) NKAP is a novel RS-related protein that interacts with RNA and RNA binding proteins. Nucleic Acids Res **42:** 3177–3193

Byrne ME (2009) A role for the ribosome in development. Trends Plant Sci **14:** 512–519

Choesmel V, Fribourg S, Aguissa-Touré AH, Pinaud N, Legrand P, Gazda HT, Gleizes PE (2008) Mutation of ribosomal protein RPS24 in Diamond-Blackfan anemia results in a ribosome biogenesis disorder. Hum Mol Genet **17:** 1253–1263

Clough SJ, Bent AF (1998) Floral dip: A simplified method for *Agrobacterium*-mediated transformation of *Arabidopsis thaliana*. Plant J **16:** 735–743

Curtis MD, Grossniklaus U (2003) A Gateway cloning vector set for high-throughput functional analysis of genes in planta. Plant Physiol **133:** 462–469

de la Cruz J, Kressler D, Tollervey D, Linder P (1998) Dob1p (Mtr4p) is a putative ATP-dependent RNA helicase required for the 3′ end formation of 5.8S rRNA in *Saccharomyces cerevisiae*. EMBO J **17:** 1128–1140

Dinman JD (2009) The eukaryotic ribosome: Current status and challenges. J Biol Chem **284:** 11761–11765

Durut N, Abou-Ellail M, Pontvianne F, Das S, Kojima H, Ukai S, de Bures A, Comella P, Nidelet S, Rialle S, et al (2014) A duplicated *NUCLEOLIN* gene with antagonistic activity is required for chromatin organization of silent 45S rDNA in Arabidopsis. Plant Cell **26:** 1330–1344

Falk S, Tants JN, Basquin J, Thoms M, Hurt E, Sattler M, Conti E (2017) Structural insights into the interaction of the nuclear exosome helicase Mtr4 with the preribosomal protein Nop53. RNA **23:** 1780–1787

Ferreira-Cerca S, Pöll G, Gleizes PE, Tschochner H, Milkereit P (2005) Roles of eukaryotic ribosomal proteins in maturation and transport of pre-18S rRNA and ribosome function. Mol Cell **20:** 263–275

Granato DC, Gonzales FA, Luz JS, Cassiola F, Machado-Santelli GM, Oliveira CC (2005) Nop53p, an essential nucleolar protein that interacts with Nop17p and Nip7p, is required for pre-rRNA processing in *Saccharomyces cerevisiae*. FEBS J **272:** 4450–4463

Hang R, Liu C, Ahmad A, Zhang Y, Lu F, Cao X (2014) Arabidopsis protein arginine methyltransferase 3 is required for ribosome biogenesis by affecting precursor ribosomal RNA processing. Proc Natl Acad Sci USA **111:** 16190–16195

Horiguchi G, Mollá-Morales A, Pérez-Pérez JM, Kojima K, Robles P, Ponce MR, Micol JL, Tsukaya H (2011) Differential contributions of ribosomal protein genes to *Arabidopsis thaliana* leaf development. Plant J **65:** 724–736

Jackson RN, Klauer AA, Hintze BJ, Robinson H, van Hoof A, Johnson SJ (2010) The crystal structure of Mtr4 reveals a novel arch domain required for rRNA processing. EMBO J **29:** 2205–2216

Kilchert C, Wittmann S, Vasiljeva L (2016) The regulation and functions of the nuclear RNA exosome complex. Nat Rev Mol Cell Biol **17:** 227–239

Lange H, Sement FM, Gagliardi D (2011) MTR4, a putative RNA helicase and exosome co-factor, is required for proper rRNA biogenesis and development in *Arabidopsis thaliana*. Plant J **68:** 51–63

Lange H, Zuber H, Sement FM, Chicher J, Kuhn L, Hammann P, Brunaud V, Bérard C, Bouteiller N, Balzergue S, et al (2014) The RNA helicases AtMTR4 and HEN2 target specific subsets of nuclear transcripts for degradation by the nuclear exosome in *Arabidopsis thaliana*. PLoS Genet **10:** e1004564

Lee S, Kim JY, Kim YJ, Seok KO, Kim JH, Chang YJ, Kang HY, Park JH (2012) Nucleolar protein GLTSCR2 stabilizes p53 in response to ribosomal stresses. Cell Death Differ **19:** 1613–1622

Liu Y, Tabata D, Imai R (2016) A cold-inducible DEAD-box RNA helicase from *Arabidopsis thaliana* regulates plant growth and development under low temperature. PLoS ONE **11:** e0154040

Mancinelli AL (1990) Interaction between light quality and light quantity in the photoregulation of anthocyanin production. Plant Physiol **92:** 1191–1195

Micol-Ponce R, Aguilera V, Ponce MR (2014) A genetic screen for suppressors of a hypomorphic allele of Arabidopsis *ARGONAUTE1*. Sci Rep **4:** 5533

Micol-Ponce R, Sarmiento-Mañús R, Ruiz-Bayón A, Montacié C, Sáez-Vasquez J, Ponce MR (2018) Arabidopsis RIBOSOMAL RNA PROCESSING7 is required for 18S rRNA maturation. Plant Cell **30:** 2855–2872

Montacié C, Durut N, Opsomer A, Palm D, Comella P, Picart C, Carpentier MC, Pontvianne F, Carapito C, Schleiff E, et al (2017) Nucleolar proteome analysis and proteasomal activity assays reveal a link between nucleolus and 26S proteasome in *A. thaliana*. Front Plant Sci **8:** 1815

Palade GE (1955) Studies on the endoplasmic reticulum. II. Simple dispositions in cells in situ. J Biophys Biochem Cytol **1:** 567–582

Parry G, Ward S, Cernac A, Dharmasiri S, Estelle M (2006) The Arabidopsis SUPPRESSOR OF AUXIN RESISTANCE proteins are nucleoporins with an important role in hormone signaling and development. Plant Cell **18:** 1590–1603

Pasternak T, Tietz O, Rapp K, Begheldo M, Nitschke R, Ruperti B, Palme K (2015) Protocol: An improved and universal procedure for whole-mount immunolocalization in plants. Plant Methods **11:** 50

Paul B, Montpetit B (2016) Altered RNA processing and export lead to retention of mRNAs near transcription sites and nuclear pore complexes or within the nucleolus. Mol Biol Cell **27:** 2742–2756

Pérez-Pérez JM, Rubio-Díaz S, Dhondt S, Hernández-Romero D, Sánchez-Soriano J, Beemster GT, Ponce MR, Micol JL (2011) Whole organ, venation and epidermal cell morphological variations are correlated in the leaves of Arabidopsis mutants. Plant Cell Environ **34:** 2200–2211

Petricka JJ, Nelson TM (2007) Arabidopsis nucleolin affects plant development and patterning. Plant Physiol **144:** 173–186

Phipps KR, Charette J, Baserga SJ (2011) The small subunit processome in ribosome biogenesis: Progress and prospects. Wiley Interdiscip Rev RNA **2:** 1–21

Ponce MR, Quesada V, Micol JL (1998) Rapid discrimination of sequences flanking and within T-DNA insertions in the Arabidopsis genome. Plant J **14:** 497–501

Ponce MR, Robles P, Lozano FM, Brotóns MA, Micol JL (2006) Low-resolution mapping of untagged mutations. Methods Mol Biol **323:** 105–113

Ponce MR, Robles P, Micol JL (1999) High-throughput genetic mapping in *Arabidopsis thaliana*. Mol Gen Genet **261:** 408–415

Pontvianne F, Matía I, Douet J, Tourmente S, Medina FJ, Echeverria M, Sáez-Vásquez J (2007) Characterization of *AtNUC-L1* reveals a central role of nucleolin in nucleolus organization and silencing of *AtNUC-L2* gene in Arabidopsis. Mol Biol Cell **18:** 369–379

Robles P, Fleury D, Candela H, Cnops G, Alonso-Peral MM, Anami S, Falcone A, Caldana C, Willmitzer L, Ponce MR, et al (2010) The *RON1/FRY1/SAL1* gene is required for leaf morphogenesis and venation patterning in Arabidopsis. Plant Physiol **152:** 1357–1372

Robles P, Micol JL (2001) Genome-wide linkage analysis of Arabidopsis genes required for leaf development. Mol Genet Genomics **266:** 12–19

Rosado A, Li R, van de Ven W, Hsu E, Raikhel NV (2012) Arabidopsis ribosomal proteins control developmental programs through translational regulation of auxin response factors. Proc Natl Acad Sci USA **109:** 19537–19544

Sáez-Vásquez J, Delseny M (2019) Ribosome biogenesis in plants: From functional 45S ribosomal DNA organization to ribosome assembly factors. Plant Cell **31:** 1945–1967

Sánchez-García AB, Aguilera V, Micol-Ponce R, Jover-Gil S, Ponce MR (2015) Arabidopsis *MAS2*, an essential gene that encodes a homolog of animal NF-κ B activating protein, is involved in 45S ribosomal DNA silencing. Plant Cell **27:** 1999–2015

Sasaki M, Kawahara K, Nishio M, Mimori K, Kogo R, Hamada K, Itoh B, Wang J, Komatsu Y, Yang YR, et al (2011) Regulation of the MDM2-P53 pathway and tumor growth by PICT1 via nucleolar RPL11. Nat Med **17:** 944–951

Seiser RM, Sundberg AE, Wollam BJ, Zobel-Thropp P, Baldwin K, Spector MD, Lycan DE (2006) Ltv1 is required for efficient nuclear export of the ribosomal small subunit in *Saccharomyces cerevisiae*. Genetics **174:** 679–691

Simm S, Fragkostefanakis S, Paul P, Keller M, Einloft J, Scharf KD, Schleiff E (2015) Identification and expression analysis of ribosome biogenesis factor co-orthologs in *Solanum lycopersicum*. Bioinform Biol Insights **9:** 1–17

Slomovic S, Laufer D, Geiger D, Schuster G (2006) Polyadenylation of ribosomal RNA in human cells. Nucleic Acids Res **34:** 2966–2975

Suzuki A, Kogo R, Kawahara K, Sasaki M, Nishio M, Maehama T, Sasaki T, Mimori K, Mori M (2012) A new PICTure of nucleolar stress. Cancer Sci **103:** 632–637

Sydorskyy Y, Dilworth DJ, Halloran B, Yi EC, Makhnevych T, Wozniak RW, Aitchison JD (2005) Nop53p is a novel nucleolar 60S ribosomal subunit biogenesis protein. Biochem J **388:** 819–826

Tafforeau L, Zorbas C, Langhendries JL, Mullineux ST, Stamatopoulou V, Mullier R, Wacheul L, Lafontaine DL (2013) The complexity of human ribosome biogenesis revealed by systematic nucleolar screening of pre-rRNA processing factors. Mol Cell **51:** 539–551

Thoms M, Thomson E, Baßler J, Gnädig M, Griesel S, Hurt E (2015) The exosome is recruited to RNA substrates through specific adaptor proteins. Cell **162:** 1029–1038

Thomson E, Tollervey D (2005) Nop53p is required for late 60S ribosome subunit maturation and nuclear export in yeast. RNA **11:** 1215–1224

Tomecki R, Sikorski PJ, Zakrzewska-Placzek M (2017) Comparison of preribosomal RNA processing pathways in yeast, plant and human cells: Focus on coordinated action of endo- and exoribonucleases. FEBS Lett **591:** 1801–1850

Weis BL, Kovacevic J, Missbach S, Schleiff E (2015) Plant-specific features of ribosome biogenesis. Trends Plant Sci **20:** 729–740

Wild T, Horvath P, Wyler E, Widmann B, Badertscher L, Zemp I, Kozak K, Csucs G, Lund E, Kutay U (2010) A protein inventory of human ribosome biogenesis reveals an essential function of exportin 5 in 60S subunit export. PLoS Biol **8:** e1000522

Wilson DN, Doudna Cate JH (2012) The structure and function of the eukaryotic ribosome. Cold Spring Harb Perspect Biol **4:** a011536

Zhang XR, Qin Z, Zhang X, Hu Y (2015) Arabidopsis SMALL ORGAN 4, a homolog of yeast NOP53, regulates cell proliferation rate during organ growth. J Integr Plant Biol **57:** 810–818